Long Time Scale Evolution of Collisionless Driven Reconnection in a Two-Dimensional Open System

Wenbing Pei

DOCTOR OF PHILOSOPHY

Department of Fusion Science
School of Mathematical and Physical Science
The Graduate University for Advanced Studies

2000 (School Year)

Abstract

Collisionless magnetic reconnection is a fundamental process of many dynamical phenomena with a fast and impulsive energy release observed in high temperature plasmas, such as solar flares, geomagnetic substorms and tokamak disruptions. Magnetic reconnection requires some non-ideal mechanism to break down the frozen-in constraint in a weak field region, called dissipation region, and thus allows the topological change of magnetic field. This process can lead to a sudden release of stored magnetic energy into particle energy and plasma transport in a large spatial scale. The fast and impulsive reconnection in collisionless plasmas remains one of major subjects of plasma physics and at a hot issue to date. Collisionless reconnection driven by an external plasma inflow, collisionless driven reconnection, is one of the potential candidates because reconnection rate is mainly controlled by external driving conditions. Driven reconnection is a dynamical process in an open system where there exist energy inflow and outflow through its boundaries. For an open system with a constant energy supply, we would expect two ways of time evolution in collisionless driven reconnection in a long time scale, i.e., steady and intermittent ways. Only a few particle simulations have so far been carried out to investigate dynamical process of collisionless driven reconnection. However, these studies are restricted to only early growing phase because a periodic condition is used at the downstream boundaries. Thus, which way the system selects as an evolution route remains unsolved to date.

In order to to explore long time scale behavior of collisionless driven reconnection, a full open boundary model is required. We develop a new two-dimensional particle simulation model for an open system with free conditions at the downstream boundaries on the basis of the previous version. In this model, a free physical condition is used at the downstream boundary, across which particles can freely go in and out. At the upstream boundary the driving condition can be uniquely determined by an external driving electric field which is described by two key parameters, i.e., the strength E_0 and the early non-uniformity scale x_d. Based on the newly developed open model, long time scale evolution of collisionless driven reconnection is simulated. The simulation results reveal many new features of collisionless reconnection which help us to understand the physical processes of collisionless reconnection. In this thesis, we clarify the mechanism of collisionless driven reconnection, and the relationship between the driving conditions and the long time scale

behavior of driven reconnection.

The evolution of collisionless driven reconnection depends strongly on the external driving electric field. The strength E_0 controls the reconnection rate, while the scale x_d controls the current layer shape and thus the magnetic field configuration. It is found that there are two regimes in the long time scale behavior of collisionless reconnection which is mainly controlled by the scale x_d in our simulation parameter range, i.e., steady regime and intermittent regime. In a small x_d case the system evolves toward a steady regime in which steady reconnection is realized and thus the global field topology remains unchanged. This is the first results that particle simulation discloses the existence of steady reconnection. On the other hands, in a large x_d case the system evolves into an intermittent regime in which magnetic islands are frequently excited to grow near the center of the current sheet.

The physical features of the steady reconnection is investigated. The reconnection rate in the steady regime is determined by the strength of the driving electric field E_0 even if reconnection would be triggered by microscopic particle dynamics. In other words, microscopic scale dynamics in the current sheet evolves so as to accommodate macroscopic scale dynamics in the surroundings. The dissipation region has two-scales structure corresponding to both the electron dynamics and the ion dynamics. The electron dissipation region is dominated by the electron inertia effect which controls the electron flow velocity through an electrostatic field. The ion inertia effect is responsible for breaking the ion frozen-in constraint in the ion dissipation region, while the ion meandering motion plays an important role in ion dynamics which controls the spatial structures of plasma density, ion flow velocity and ion temperature. Although the current is predominantly carried by electrons, the current layer has the half-width of the ion meandering orbit scale l_{mi}. This is because the density profile is exclusively controlled by the massive ion motion. That is, the global dynamic process of steady magnetic reconnection is dominantly controlled by ion dynamics. The electrostatic field generated through a finite Larmor radius effect is a key to coordinate the motions of electrons and ions. It leads to electron acceleration in an equilibrium current direction in the ion dissipation region and ion heating by intensifying meandering motion. Our results are in good agreement with the recent experimental results in MRX in the aspects of current layer width and ion heating [Yamada *et al.*, Phys. Plasmas 7, 1781 (2000), Hus *et al.*, Phys. Rev. Lett. 84, 3859 (2000)].

The dynamical process of collisionless reconnection in the intermittent regime is studied. The intermittent behavior is found to appear due to the frequent formation of magnetic islands as a result of the excitation of an electron microscopic instability. The detailed analysis of simulation results reveals that the island growth is caused by the current increase through the electron trapping in it, and thus the instability is triggered by electron dynamics. To shed light on the island excitation mechanism in the intermittent

regime, the effect of the driving parameters E_0 and x_d on the current layer structure and the magnetic field configuration has been explored in the regime of steady reconnection. As E_0 increases, the current layer is similarly compressed, and thus the corresponding magnetic field configuration is almost unchanged. On the contrary, as x_d increases, the current layer becomes narrow and flat in shape so that the angle between the separatrices decreases. The change of the current layer structure leads to generation of a seed island with spatial size longer than the electron meandering size in the outflow direction, which is equal to the spatial size of unmagnetized electron thermal motion. This island grows up by increasing the electric current through the electron trapping in it. Thus, in a large x_d case the system evolves into the intermittent regime in which magnetic islands is frequently formed near the original X point.

Contents

Chapter 1

Introduction

1.1 General picture of magnetic reconnection

Magnetic reconnection plays an important role in plasmas because it leads to the fast energy release from magnetic field to plasmas and the change of magnetic field topology as well. Evidence of magnetic reconnection is found in all relevant plasma environments, both space plasmas and laboratory plasmas. Solar flares and coronal mass ejections are widely studied in relation to reconnection processes [1, 2, 3]. In the magnetosphere, dayside reconnection at the magnetopause permits the solar wind plasma to enter magnetosphere [4]. The solar wind transports the reconnected field lines to the nightside across the polar cap and triggers magnetic reconnection in the magnetotail which is involved in geomagnetic storm and substorm dynamics [5, 6, 7, 8]. In addition, some of particle acceleration phenomena in galaxies [9] seem to be caused by reconnection. In tokamaks sawtooth oscillations, Mirnov oscillations and disruptions [10] are all attributed at least partly to reconnection processes. Thus, most of dynamical processes in magnetized plasmas involve magnetic reconnection.

Magnetic reconnection is a process in which the topology of magnetic field is changed. The basic picture is illustrated in Fig. 1.1. Consider magnetic topology with antiparallel field lines around a thin current sheet, as sketched in the left panel. When field lines carried by plasma move toward the current sheet and contact at some point, i.e., reconnection point (see the middle panel), they are cut and reconnected to other field lines. The reconnected field lines are then expelled from the reconnection point due to the magnetic tension (see the right panel). The reconnection point is also called X point after the shape of field lines, and the magnetic neutral point due to the magnetic field being zero at this point. The field lines forming the figure X and passing through the reconnection point are called separatrix.

Magnetic reconnection cannot take place in an ideal magnetohydrodynamic (MHD) plasma because the magnetic field is frozen in the plasma and the relative positions (or

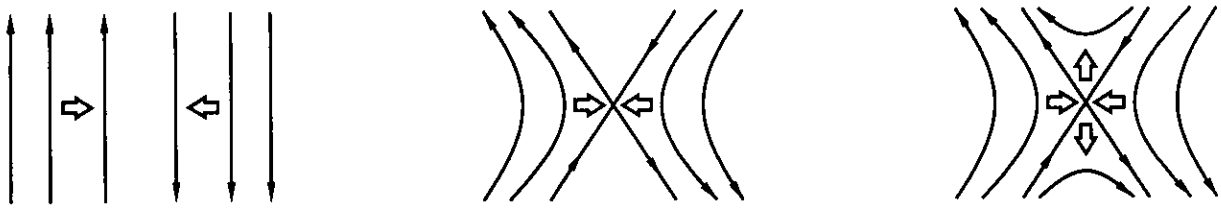

Figure 1.1: Illustration of reconnection process.

topological structure) of the fluid elements are kept unchanged. Magnetic reconnection requires the existence of a nonideal mechanism which is responsible for breaking the frozen-in constraint

$$\mathbf{E} + \frac{\mathbf{u}}{c} \times \mathbf{B} = 0, \tag{1.1}$$

where c is the speed of light, $\mathbf{u}$ is the fluid velocity and $\mathbf{E}$ and $\mathbf{B}$ are respectively electric and magnetic fields. The nonideal effect induces an out-of-plane electric field at the field null point, called reconnection electric field, which drives an electric current and allows reconnection to proceed. Most of early studies on magnetic reconnection are based on the resistive MHD model in which the nonideal process, dissipation, is provided by an electrical resistivity originating from the binary collision between electrons and ions. The induction equation for the magnetic field $\mathbf{B}$ is

$$\frac{\partial \mathbf{B}}{\partial t} = \nabla \times (\mathbf{u} \times \mathbf{B}) + \frac{c^2}{4\pi} \eta \nabla^2 \mathbf{B} \tag{1.2}$$

where η is the resistivity. The resistive dissipation, the second term on the right hand side (RHS), allows the magnetic field to diffuse across the plasma and to smooth out any local inhomogeneity, and thus it can lead to the release of the magnetic free energy and the change in magnetic topology. The first term on the RHS describes the convective motion of the field along with the plasma. The importance of the two terms is characteristized by the magnetic Reynolds number,

$$R_m = 4\pi u L_B / c^2 \eta \tag{1.3}$$

where L_B is the characteristic length of magnetic field variation. When the relation $R_m \gg 1$ holds everywhere, the diffusion term can be neglected and the plasma is fully ideal. It is evident that the diffusion term is negligible in a highly conducting plasma except for in the vicinity of reconnection point, called dissipation region, where the gradient scale of magnetic field becomes small and the in-plane component of $\mathbf{u}$ vanishes. Thus, magnetic reconnection is a localized process.

Although magnetic reconnection is a localized process, it may completely change the global field line topology, permitting the plasma transport across the magnetic field and the mixture between plasmas of different origins which would be inhibited in the absence of diffusion term. Moreover, magnetic reconnection leads to energy conversion from magnetic field into plasma. In other words, acceleration and heating of plasmas take place through magnetic reconnection. It is worthy of notice that although ideal MHD processes, such as the ideal kink instability, can also release magnetic energy quickly, the distinction is important in two aspects. Ideal MHD processes can convert magnetic energy into only kinetic energy but cannot lead to plasma heating (i.e., raise the entropy) without any dissipation. And they rarely release a significant amount of energy due to the topological constraint. In contrast, magnetic reconnection can release a much greater amount of magnetic energy so that a system can relax toward a minimum energy state by changing magnetic topology.

The research on magnetic reconnection was originated from the studies by Giovanelli in the 1940s [11, 12] to explain solar activities. Hoyle [13] and Dungey [14] applied the idea to geomagnetic phenomena. Giovanelli [11, 12] and Hoyle [13] suggested the concept of magnetic X-type null points severing as locations for plasma heating and acceleration in solar flares and substorms. Cowling [15] pointed out in 1953, that a current sheet is needed to power solar flare. Dungey [16] developed X-type collapse theory and showed the formation of current sheet during collapse. Then Sweet and Parker [17, 18] presented the first simple MHD model for steady-state reconnection. However, the Sweet-Parker reconnection rate is too slow to account for realistic application. Petschek [19] in 1964 developed slow shock model with a much smaller current sheet and predicted a much faster reconnection rate being very weakly dependent on the resistivity through the logarithmic term. Since then, more general models for fast reconnection have been developed. On the other hand, Furth, Killeen and Rosenbluth [20] in 1963 presented resistive tearing mode theory, as one of the most important developments in the reconnection theory, to explain reconnection phenomena occurring in fusion devices.

1.2 Collisionless reconnection

Magnetic reconnection can occur not only in collisional plasmas but also in collisionless plasmas provided that the magnetic field diffuses across the plasma in the presence of nonideal mechanism. In many applications of interest, the magnetic Reynolds number is quite large, for example, about 10^7 in a tokamak plasma and $10^{11} \sim 10^{13}$ in a solar coronal loop plasma, and thus the electrical resistivity based on Coulomb collision of particles is too weak to explain the observations. In general, collisionless reconnection rate is much faster than the value estimated from the collisional effect, e.g., fast energy conversion in

the impulsive phase of solar flares, and an abrupt energy release in the tokamak disruption and sawteeth oscillations. To explore this fast reconnection process remains a particular challenge to plasma physics though it has been studied for more than three decades.

In a collisionless plasma, nonideal mechanism that breaks the frozen-in constraint is generally considered to come from kinetic effects. One of them is an anomalous resistivity generated near the reconnection point through the wave-particle interaction [21, 22, 23, 24] (or the stochasticity of particle orbit). The interaction between particles carrying electric current and a wave propagating along the electric current becomes an origin of an anomalous resistivity which can also lead to collisionless reconnection. The study of this effect needs a three-dimensional treatment that is beyond the scope of the present investigation.

The others are microscale particle kinetic effects based on nongyrotropic (or so-called meandering) motion and convective motion. In a fluid description the mechanism to break the frozen-in constraint can be described by volume inertia effect (or inertia effect) and thermal inertia effect (or thermal effect), as first discussed by Vasyliunas [25]. To get insight into the nonideal effects causing violation of the frozen-in condition, let us consider the momentum equation for species s $(= i, e)$

$$\mathbf{E} + \frac{\mathbf{u}_s}{c} \times \mathbf{B} = \frac{1}{n_s q_s} \nabla \cdot \mathbf{P}_s, + \frac{m_s}{q_s} \left(\frac{\partial \mathbf{u}_s}{\partial t} + \mathbf{u}_s \cdot \nabla \mathbf{u}_s \right), \tag{1.4}$$

where $\mathbf{u}_s$, n_s, q_s, m_s, $\mathbf{P}_s$ denote velocity, number density, charge, mass and pressure tensor. Equation (1.4) should hold for all plasma species since it can be derived directly from Vlasov equation without any approximation. While the left-hand side (LHS) of Eq. (1.4) describes the frozen-in state, the terms on the RHS refer to nonideal mechanisms, i.e., the thermal effect based on anisotropic pressure and the inertia effect of the bulk flow, respectively. It is worth pointing out that in two dimensions (2D), a scalar pressure or a pressure tensor with only diagonal elements dose not contribute itself to an reconnection electric field and also dose not cause reconnection [26]. This point can be seen from the magnetic induction equation in which the term associated with the scalar pressure or the diagonal pressure elements disappears when substituted into Faraday's equation. Only the off-diagonal elements of pressure tensor associated with particle meandering motion can balance the reconnection field near the X point [25, 27, 28, 29, 30, 31] because the off-diagonal pressure tensor caused by a skewed velocity distribution of particles acts as viscosity, causing the momentum transport and allowing a relative motion of different species to form the electric current [32].

The relative importance of these terms is estimated by their characteristic scales. The process with the largest scale length will dominate the breaking process. The inertia term has an effect in a collisionless skin depth, δ_s $(= c/\omega_{ps})$, where ω_{ps} is the plasma frequency of species s. The thermal effect becomes important when the dissipation region

is of the scale comparable to the Larmor radius, ρ_s ($= v_{ts}/\omega_{cs}$), where v_{ts} is the thermal velocity and ω_{cs} the local cyclotron frequency of species s. Both characteristic scales are proportional to $m_s^{1/2}$. Therefore, the ion kinetic effects are of much larger scales than electron effects.

The literatures often involve a term of the Hall effect [33, 34, 35, 36]. This is an MHD concept appearing in the generalized Ohm's law

$$\mathbf{E} + \frac{\mathbf{u}}{c} \times \mathbf{B} = \frac{\mathbf{j} \times \mathbf{B}}{nec} - \frac{1}{ne} \nabla \cdot \mathbf{P}_e - \frac{m_e}{e} \left(\frac{\partial \mathbf{u}_e}{\partial t} + \mathbf{u}_e \cdot \nabla \mathbf{u}_e \right), \tag{1.5}$$

where the first term on the RHS is called the Hall term, $\mathbf{u}$ is the fluid flow velocity, and $\mathbf{j}$ the current density. When the Hall term dominates over the other terms on the RHS, Eq. (1.5) reduces to

$$\mathbf{E} + \frac{\mathbf{u}}{c} \times \mathbf{B} = \frac{\mathbf{j} \times \mathbf{B}}{nec}. \tag{1.6}$$

By using the relations $\mathbf{j} = en(\mathbf{u}_e - \mathbf{u}_i)$ and $\mathbf{u} \approx \mathbf{u}_i$, we rewrite Eq. (1.6) as

$$\mathbf{E} + \frac{\mathbf{u}_e}{c} \times \mathbf{B} = 0. \tag{1.7}$$

Thus, the Hall effect implies that the magnetic field is frozen into the electron fluid [Eq. (1.7)], but not the ion fluid [Eq. (1.6)]. In other words, the ions are unmagnetized due to the Hall term. If Eq. (1.6) is substituted into the equation of ion momentum, Eq. (1.4) with $s = i$, we have

$$\frac{\mathbf{j} \times \mathbf{B}}{nec} = \frac{1}{ne} \nabla \cdot \mathbf{P}_i, + \frac{m_i}{e} \left(\frac{\partial \mathbf{u}_i}{\partial t} + \mathbf{u}_i \cdot \nabla \mathbf{u}_i \right). \tag{1.8}$$

This equation means that the Hall term itself dose not tell us which effect, ion inertia or ion thermal effect, allows ion motion to deviate from the field.

In a collisionless plasma the dissipation region develops to form a multiscale structure associated with the electron and ion scales [33, 34, 35, 36, 37]. Outside of the dissipation region both electrons and ions move together because they are magnetized and ideal. Suppose that the plasma inflow is driven toward the neutral sheet from the outer frozen-in region. As soon as ions move into the region of an ion scale length, ion motion decouples from the magnetic field because of Hall effect (either its thermal effect or its inertia effect) and ions are diverted in the direction of outflow from the X point, while the electrons remain magnetized until they move into the region of electron scale length, c/ω_{pe} or ρ_e, and decouple from the magnetic field. As a result of decoupling of electron and ion motion, an electrostatic field is built in the inflow direction. This electric field accelerates the ions in the inflow direction, but causes an $\mathbf{E} \times \mathbf{B}$ drift motion of electrons in the out-of-plane direction. Therefore, a current layer is actually formed in the ion dissipation region.

1.3 Driven reconnection

Magnetic reconnection is often divided into spontaneous reconnection and driven reconnection. Spontaneous reconnection is triggered due to internal instabilities such as the collisionless tearing instability [20, 38, 39, 40, 41, 42, 43, 44, 45, 46] in the absence of an external driving source (i.e., no energy inflow from the boundary). Driven reconnection is related to an open system where plasma inflow and magnetic field are supplied from upstream boundaries. In this research we study driven reconnection underlying the following reasons.

Most of active plasma phenomena in nature and laboratory are relevant to driven reconnection where a plasma flow is the primary cause of magnetic reconnection. It is a common case in nature that the flow energy can be larger than the magnetic energy. In the solar wind-magnetosphere coupling system, for example, the solar wind drives reconnection at the magnetopause. Reconnection allows the solar wind plasma to enter magnetosphere. When the plasma is accelerated and reaches the magnetotail, it gives rise to a second reconnection. A similar example is the interaction between accreting plasma and a magnetic star. In magnetic confinement devices, the plasma current is a major source of free energy, so that a plasma flow resulting from various current-driven instabilities can lead to deformation of the magnetic configuration.

Driven reconnection is a potential candidate of fast reconnection because reconnection rate is mainly controlled by external driving conditions. The resistive MHD simulation by Sato and Hayashi [47] reveals that driven reconnection rate is relatively independent of resistivity but strongly dependent on the amplitude of the driving plasma flow. This conclusion should also be applicable to collisionless driven reconnection since reconnection rate is also determined by the ion inflow velocity which is controlled by the external conditions. If this inference is right, one can say that collisionless reconnection can be a fast process, which is important to understand many realistic reconnection phenomena. Therefore, this point is one of the motivations of the present research.

Although magnetic reconnection is a localized process, it gives rise to plasma transport in a global scale. In this sense, the evolution of spontaneous reconnection is also affected by other physical processes outside the dissipation region. Thus, driven process is important in considering magnetic reconnection in large time and space scales.

In order to clarify microscopic mechanism of collisionless reconnection, we are forced to restrict our simulation domain to a small region including the dissipation region. A driven system may be regarded as a section of whole reconnection system so as to keep higher spatial resolution of the dissipation region with microscopic scales under the condition of the limited computer resource.

1.4 Study status of collisionless reconnection

Magnetic reconnection has been studied based on satellite observations [5, 6, 7, 8], laboratory plasma experiments [48, 49, 50], theoretical analysis [38, 39], and computer simulations [27, 28, 29, 30, 31, 33, 34, 35, 37] in past decades. Although these studies have advanced the understanding of magnetic reconnection, the fundamental physics of fast reconnection remains unknown to date. Many recent studies of collisionless reconnection focus on the understanding of reconnection mechanism, in particular, reconnection rate, dissipation region size, current layer width and their relation with electron and ion dynamics.

Numerical simulations have been developed as one of the most powerful tools for reconnection study. Full particle simulation is required to address the problem of collisionless reconnection. A considerable amount of effort has been made [27, 28, 29, 30, 45, 51]. Because of the limit of computer resources, however, various simple models, such as Hall-MHD simulation (with massless electrons and scalar pressure) [52], two-fluid simulation (with scalar pressure) [33, 34, 53] and hybrid simulations (ion particles and electron fluid with/without electron inertia/pressure tenser) [31, 35, 37, 54, 55], have widely been used in place of full particle simulation. These simple model cannot often account for all potential kinetic effects, as shown in Eq. (1.4). In the Hall-MHD and conventional hybrid models all the electron non-ideal terms are removed, and reconnection is supported by an ad hoc anomalous resistivity or/and by a numerical resistivity. The detailed discussion of these models are referred to the paper [31] and references therein.

Most simulations focus on the problem of non-driven collisionless reconnection in a closed system. An important conclusion from recent studies [30, 31, 33, 34, 35, 37] is that the reconnection rate is controlled by the ion dynamics based on the Hall effect which is faster than on the resistivity, and is essentially independent of the electron dynamics by which the electron frozen-in condition is broken. The corresponding current layer width is, however, scaled by the electron skin depth δ_e or gyro-radius ρ_e.

Because of numerical difficulties, very few simulations based on Hall-MHD model [52], two-fluid model [53], the hybrid model [54] and particle simulation [27, 28] involve collisionless driven reconnection which refers to an open system. Horiuchi and Sato [27, 28] have firstly performed the particle simulations of collisionless driven reconnection. They found that the early evolution of collisionless reconnection is dependent not only on the internal microscopic processes such as electron dynamics and ion dynamics, but also on the external driving condition. When the current layer shrinks from the ion orbit size to the electron orbit size, reconnection transits from slow growth to fast growth, and electrons are heated. The global evolution of reconnection is controlled mainly by the ion dynamics. The reconnection rate is in proportion to the driving electric field. However, their studies are limited to an early ramp-up phase because a periodic condition is used

at the downstream boundary.

On the other hand, experimental studies in the Magnetic Reconnection Experiment (MRX) have found that the current layer width is about $0.4\delta_i \sim \rho_i$ [48] and that the significant nonclassical ion heating occurs in the current layer [48, 49].

1.5 Steady reconnection and intermittent behavior

Reconnection is often discussed with steady models, such as Sweet-Parker current sheet model [17, 18] and Petschek slow shock model [19]. The question is whether steady reconnection is realized in a realistic system. For an open system with a constant energy supply, the steady state is certainly a possible tendency of evolution. However, the steady state is not always realized even if there exists a steady state. For example, Kitabata *et al* [56] and Amo *et al* [57] have demonstrated intermittent phenomena in the magnetic reconnection processes by using resistive MHD simulation. Intermittent behavior has also been observed by Hall-MHD and two-fluid simulations [52, 53]. There are two factors that disrupt the steady state. One comes from the disparity of internal physical process and external physical condition. The steady reconnection is realized when the reconnection rate is balanced with the external driving flow rate. That is, the internal processes (electron dynamics and ion dynamics) should adjust themselves to accommodate the external driving condition, because magnetic reconnection is controlled by both the internal microscopic process and the external driving condition. However, the adjustment is limited. Beyond this limit, there is no steady state. The other is due to an instability. If such a steady state itself is unstable due to some instabilities such as the tearing instability, or if an instability can be excited in the process of system evolution, the reconnection can hardly tend toward this steady state, but often behaves intermittently. Thus the evolution of collisionless driven reconnection depends closely on the rate and spatial pattern of driving flow.

How collisionless driven reconnection evolves in a long time scale and what dependence of its evolution behavior on the external driving conditions remain unsolved to date. It appears that reconnection may operate in entirely different ways for different plasma parameters and for different external driving conditions. Steady reconnection may be allowed in some cases, forbidden in others, with intermediate situations involving impulsive or pulsative events.

1.6 Purpose and outline

The purpose of the present work is to explore long time scale evolution of collisionless driven reconnection by means of 2D particle simulation. We will clarify the mechanism

of collisionless driven reconnection, and the relationship between the driving conditions and the long time scale behavior of driven reconnection.

For this purpose a completely open system model is needed. Thus, we develop a new 2D particle simulation model for an open system with free conditions at the downstream boundaries on the basis of the previous version [28]. The simulation model and numerical method are described in Chapter 2. By using this newly developed model, we perform particle simulation in a long time scale and investigate the influence of the external driving conditions, i.e., the rate and spatial pattern of driving flow, on the collisionless reconnection process in a long time scale. An overview of results are given in Chapter 3. We find driven reconnection evolves in two ways, i.e., in steady and intermittent regimes. Chapter 4 is devoted to the analysis of reconnection mechanism in the steady regime with the focus on the electron dynamics and ion dynamics. On this basis we explore the mechanism that leads to intermittent phenomena in Chapter 5. Finally, a conclusion is given in Chapter 6.

Chapter 2

Simulation Model

The particle simulation is one of the most effective methods to study collisionless plasma problems. In order to study long time scale evolution of collisionless driven reconnection, we have developed a two and half dimensional explicit electromagnetic particle simulation code for an open system based on the previous version [28]. The simulation is performed in the x-y plane. Plasma flows and their carring magnetic fluxes are driven symmetrically into the system from the top and bottom upstream boundaries ($y = \pm y_b$). The driving condition can be uniquely determined by an out-of-plane electric field E_{zd} since both electrons and ions are magnetized outside the dissipation region. A free physical condition is used at the left and right downstream boundaries ($x = \pm x_b$), across which particles can flow in or out. Therefore, the total number of particles in the system changes with time, but the charge neutrality condition is kept to be satisfied. In this chapter, we will describe the open boundary model for the particle simulation in details.

2.1 Basic equations

In particle simulation the basic equations consist of the Newton-Lorentz equations of motion for particles and the Maxwell equations for field quantities. The Newton-Lorentz equations of motion are written as

$$\frac{d(\gamma_k \mathbf{v}_k)}{dt} = \frac{q_k}{m_k}(\mathbf{E} + \frac{\mathbf{v}_k}{c} \times \mathbf{B}), \tag{2.1}$$

$$\frac{d\mathbf{x}_k}{dt} = \mathbf{v}_k, \tag{2.2}$$

$$\gamma_k = 1/\sqrt{1 - v_k^2/c^2}, \tag{2.3}$$

where $\mathbf{x}_k$, $\mathbf{v}_k$, m_k, q_k and γ_k are the position, the velocity, the rest mass, the charge and the relativistic factor of the k-th particle, respectively. The Maxwell equations are

$$\frac{1}{c}\frac{\partial \mathbf{B}}{\partial t} = -\nabla \times \mathbf{E}, \tag{2.4}$$

$$\frac{1}{c}\frac{\partial \mathbf{E}}{\partial t} = \nabla \times \mathbf{B} - \frac{4\pi}{c}\mathbf{j}, \tag{2.5}$$

$$\nabla \cdot \mathbf{E} = 4\pi\rho, \tag{2.6}$$

$$\nabla \cdot \mathbf{B} = 0, \tag{2.7}$$

where $\mathbf{E}$ and $\mathbf{B}$ are the electric and magnetic fields. The current density $\mathbf{j}(\mathbf{x}, \mathrm{t})$ and the charge density $\rho(\mathbf{x}, t)$ are obtained by summing over all the particles, namely,

$$\mathbf{j}(\mathbf{x}, t) = \sum_k q_k \mathbf{v}_k(t) S[\mathbf{x} - \mathbf{x}_k(t)] \tag{2.8}$$

$$\rho(\mathbf{x}, t) = \sum_k q_k S[\mathbf{x} - \mathbf{x}_k(t)] \tag{2.9}$$

where $S(\mathbf{x})$ is the particle shape factor [58] which can be interpreted as the charge distribution of a particle.

The electric and magnetic fields described by Eqs. (2.4)-(2.7), in principle, may include long-range macroscopic fields and short-range microscopic fluctuation fields. The long-range interaction gives rise to collective behaviors, such as modes involving coherent motions of many particles with the wavelengths larger than the Debye length. The short-range interaction is related to collision. For plasmas of interest, the collective effects is much more important than collisional effects. In particle simulation, thus, Eqs. (2.4)-(2.7) actually describe the macroscopic electric and magnetic fields in the presence of the macroscopic current and charge densities by means of the spatial average over the short-range distance (e.g., the Debye length). To realize this, the method of finite-size particles (called superparticle) is introduced, which makes particle simulation feasible with finite particle number much less than in practice.

It is noteworthy that only the first two Maxwell equations are completely independent. In fact, the divergence of Eq. (2.4) gives rise to

$$\frac{\partial}{\partial t}(\nabla \cdot \mathbf{B}) = \nabla \cdot \frac{\partial \mathbf{B}}{\partial t} = -c\nabla \cdot \nabla \times \mathbf{E} \equiv 0 \tag{2.10}$$

which means that Eq. (2.7) always holds if it is satisfied initially. Similarly, from Eq. (2.5) we have

$$\frac{\partial}{\partial t}(\nabla \cdot \mathbf{E} - 4\pi\rho) = 4\pi(\nabla \cdot \mathbf{j} - \frac{\partial \rho}{\partial t}), \tag{2.11}$$

that is, Eq. (2.6) remains satisfied if $\mathbf{j}$ and ρ satisfy the continuity equation and Eq. (2.6) holds initially. However, $\mathbf{j}$ and ρ given by Eqs. (2.8)-(2.9) do not exactly satisfy the continuity equation in numerical simulation because of applicability limit of numerical techniques such as a finite sized mesh and weighting [58].

Thus in our simulation model we solve the first two Maxwell equations (2.4)-(2.5) for $\mathbf{E}$ and $\mathbf{B}$, and then adjust $\mathbf{E}$ to $\mathbf{E}'$ by correcting the electrostatic part in order to satisfy

Eq. (2.6). The Boris-type correction [58] is used as

$$\mathbf{E}' = \mathbf{E} - \nabla\delta\phi, \tag{2.12}$$

$$\nabla^2\delta\phi = \nabla\cdot\mathbf{E} - \rho. \tag{2.13}$$

2.2 Numerical scheme

The equations of motion and the Maxwell equations are solved in the explicit finite difference scheme in the x-y plane with rectangular grids. The particles are scattered around within the grid. The field quantities $\mathbf{E}$ and $\mathbf{B}$ and the sources $\mathbf{j}$ and ρ are defined at the center of grid denoted by (i, j). Both particles and fields are advanced by a second-order leap-frog algorithm. The simulation process from time step n to n+1 and the temporal layout of field and particle quantities are shown in Figure 2.1.

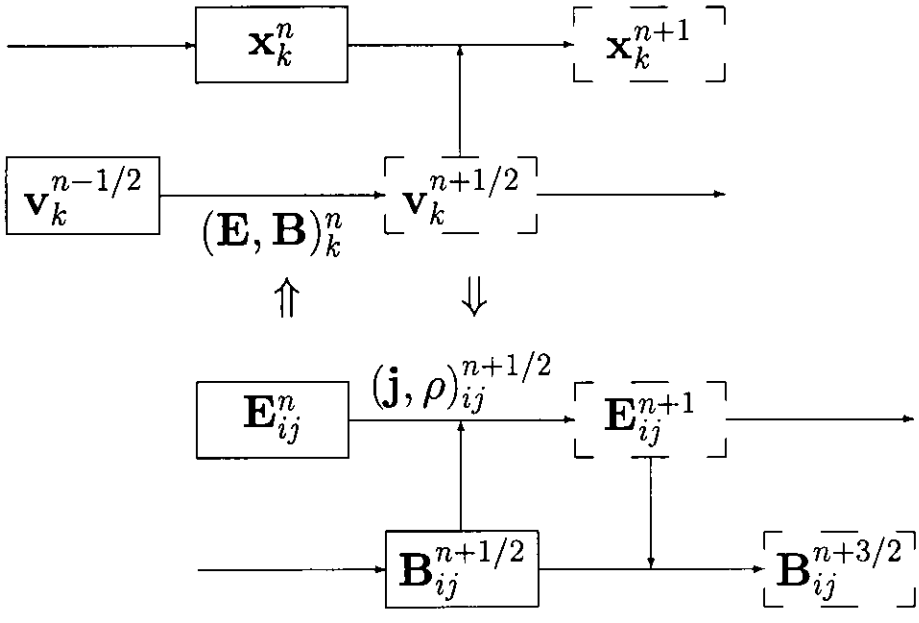

Figure 2.1: Sketch of simulation process from time step n to n+1 where the known quantities are marked by the solid boxes and the unknown by the dashed boxes.

2.2.1 Integration of the equations of motion

The difference scheme of particle motion equation (2.1) is

$$\frac{\mathbf{u}^{n+1/2}-\mathbf{u}^{n-1/2}}{\Delta t}=\frac{q}{m}\left(\mathbf{E}^{n}+\frac{\mathbf{u}^{n+1/2}+\mathbf{u}^{n-1/2}}{2c\gamma^{n}}\times\mathbf{B}^{n}\right), \tag{2.14}$$

where the superscripts stand for the time labels, and we ignore the subscript k labeling particles for convenience and use $\mathbf{u}\equiv\gamma\mathbf{v}$ rather than $\mathbf{v}$. $\mathbf{E}$ and $\mathbf{B}$ should be the values at the position of a particle which are interpolated from the values at the grid position. In Eq. (2.14) we need to specify only $(\gamma^{n})^{2}=1+(u^{n}/c)^{2}$. Centering of γ^{n} is easily determined from the Boris' method [58]. Let us define the quantities $\mathbf{u}^{+}$ and $\mathbf{u}^{-}$ as

$$\mathbf{u}^{n-1/2}=\mathbf{u}^{-}-\frac{q\mathbf{E}^{n}\Delta t}{2m} \tag{2.15}$$

$$\mathbf{u}^{n+1/2}=\mathbf{u}^{+}+\frac{q\mathbf{E}^{n}\Delta t}{2m} \tag{2.16}$$

Substituting Eqs. (2.15) and (2.16) into Eq. (2.14), we obtain

$$\frac{\mathbf{u}^{+}-\mathbf{u}^{-}}{\Delta t}=\frac{q}{2\gamma^{n}mc}(\mathbf{u}^{+}+\mathbf{u}^{-})\times\mathbf{B}^{n} \tag{2.17}$$

which describes a rotation from $\mathbf{u}^{-}$ to $\mathbf{u}^{+}$ about a axis parallel to $\mathbf{B}^{n}$ through an angle $\theta=-2\tan^{-1}(qB^{n}\Delta t/2\gamma^{n}mc)$. Because the relations $u^{n}=|\mathbf{u}^{-}|=|\mathbf{u}^{+}|$ hold from Eq. (2.17), we can specify γ^{n} from the known quantities by using Eq. (2.15). According to geometry relationship of rotation, $\mathbf{u}^{+}$ can be described by

$$\mathbf{u}'=\mathbf{u}^{-}+\mathbf{u}^{-}\times\mathbf{t} \tag{2.18}$$

$$\mathbf{u}^{+}=\mathbf{u}^{-}+\mathbf{u}'\times\mathbf{s} \tag{2.19}$$

with $\mathbf{t}=q\mathbf{B}^{n}\Delta t/2\gamma^{n}mc$ and $\mathbf{s}=2\mathbf{t}/(1+t^{2})$.

From Eqs. (2.15)-(2.19) we get the relations

$$\mathbf{v}^{n+1/2}=(\mathbf{u}/\gamma)^{n+1/2}=\left(\frac{u}{1+u^{2}/c^{2}}\right)^{n+1/2}, \tag{2.20}$$

and then advance the position to the future by one time-step Δt according to

$$\mathbf{x}^{n+1}=\mathbf{x}^{n}+\mathbf{v}^{n+1/2}\Delta t. \tag{2.21}$$

2.2.2 Integration of the field equations

The difference form of Maxwell equations (2.4)-(2.5) can be written out using the centered differencing scheme, for example, the x components being

$$\frac{E_{xij}^{n+1}-E_{xij}^{n}}{c\Delta t}=\frac{B_{zij+1}^{n+1/2}-B_{zij-1}^{n+1/2}}{2\Delta y}-\frac{4\pi}{c}j_{xij}^{n+1/2}, \tag{2.22}$$

$$\frac{B_{xij}^{n+3/2}-B_{xij}^{n+1/2}}{c\Delta t}=-\frac{E_{zij+1}^{n+1}-E_{zij-1}^{n+1}}{2\Delta y}, \tag{2.23}$$

where the subscripts i and j denote the labels of 2D space grids. When $\mathbf{E}^n$ and $\mathbf{B}^{n+1/2}$ are known, $\mathbf{E}^{n+1}$ is determined. $\mathbf{B}^{n+3/2}$ is then advanced similarly.

The time-step width Δt is chosen to satisfy the Courant-Friedrichs-Lewy (CFL) condition [59] for the electromagnetic wave in vacuum so as to make the explicit scheme stable.

2.2.3 Weighting

It is necessary to calculate the charge and current densities on the discrete grids from the particle positions and velocities when we solve the Maxwell equations and to calculate the forces on the particles from the fields on the grids when we solve the particle motion equations. These calculations are called weighting, which implies some form of interpolation among the grid centers nearest the particle. The former is obtained from Eqs. (2.8)-(2.9)

$$\mathbf{j}_{ij} = \sum_k q_k \mathbf{v}_k(t) S_{ij}(\mathbf{x}_k), \tag{2.24}$$

$$\rho_{ij} = \sum_k q_k S_{ij}(\mathbf{x}_k), \tag{2.25}$$

$$S_{ij}(\mathbf{x}_k) = \frac{1}{\Delta x \Delta y} \int_{y_j-\Delta y/2}^{y_j+\Delta y/2} dy \int_{x_i-\Delta x/2}^{x_i+\Delta x/2} dx\, S[\mathbf{x} - \mathbf{x}_k(t)] \tag{2.26}$$

The latter is interpolated from the fields on the grids as

$$\mathbf{E}_k = \Delta x \Delta y \sum_{i,j} \mathbf{E}_{ij} S_{ij}(\mathbf{x}_k), \tag{2.27}$$

$$\mathbf{B}_k = \Delta x \Delta y \sum_{i,j} \mathbf{B}_{ij} S_{ij}(\mathbf{x}_k). \tag{2.28}$$

The same weighting function S_{ij} is used in order to avoid excitation of a self-force (i.e., a particle accelerates itself) [58].

Note that S_{ij}, the average of S over the grid (i,j), is quite different from S. S_{ij} is the contribution of particle with shape of S to the density on grid (i,j), which is interpreted as the particle density distribution observed at grid point (i,j) as a particle moves into this cell. Figure 2.2 shows the zeroth-, first- and second-order weighting S_i and the corresponding particle (cloud) shapes S in one-dimensional (1D) case. For example, the zeroth-order weighting corresponds to the point particles whose shape factor S is a δ-function. As a particle moves through a grid centered at X_i, the observer (or density detector) observes that the particle has a rectangular shape S_i with a width of Δx rather than that of a point particle, S. S_i may be interpreted as the effective particle shape. This is a natural consequence due to the use of spatial grid. As seen from Fig. 2.2, the effective particle size observed is bigger by Δx than that of itself in all the cases. In other words, in the sense of grid the weighting process smooths out the density and current fluctuations,

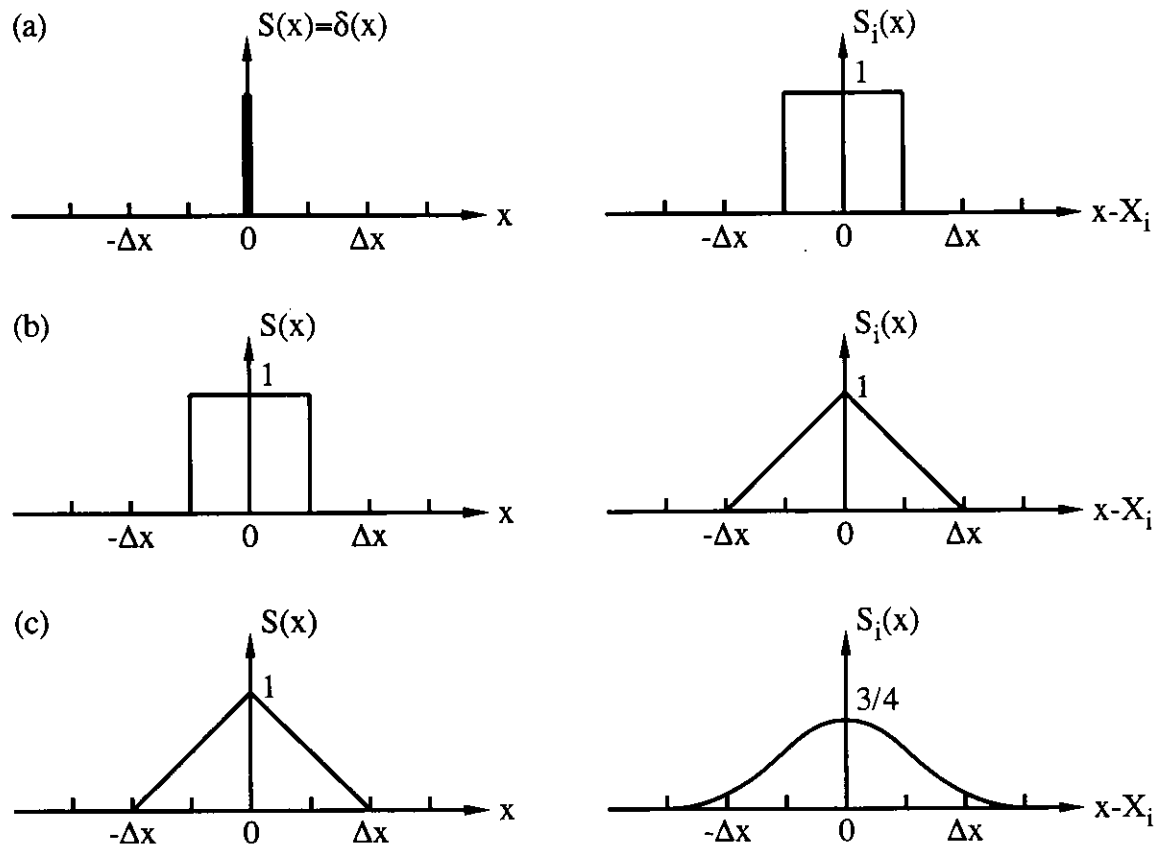

Figure 2.2: (a) zeroth-order (b) first-order and (c) second-order (quadratic spline) weighting S_i and the corresponding particle (cloud) shapes S in one-dimensional case.

and thus reduces the numerical noise. Evidently higher-order weighting rounds off further the roughness in particle shape and reduces the simulation noise more effectively.

In the present simulation we choose the second-order weighting by making use of quadratic spline. The particle shape S is a triangle with the base length of $2\Delta x$ centered at x_k in the x direction. Its contribution to charge density is assigned to three grids

$$S_i(x_k) = \frac{1}{\Delta x}\left[\frac{3}{4} - \left(\frac{x_k - X_i}{\Delta x}\right)^2\right] \tag{2.29}$$

$$S_{i\pm1}(x_k) = \frac{1}{2\Delta x}\left[\frac{1}{2} \pm \frac{x_k - X_i}{\Delta x}\right]^2 \tag{2.30}$$

where i is the nearest grid point. In the 2D case, the weighting is composed of the factor of each dimension

$$S_{ij}(\mathbf{x}_k) = S_i(x_k)S_j(y_k). \tag{2.31}$$

2.3 Boundary condition

Now, we specify the driving conditions at the upstream boundaries ($y = \pm y_b$) and the free conditions at the downstream boundaries ($x = \pm x_b$) for both field quantities and particle quantities.

2.3.1 Field quantities

In order to solve the maxwell equations, the appropriate boundary conditions are required. The problem is what boundary conditions are needed to ensure that the equations have a unique and determinate solution.

In a 2D problem the fields may be divided into transverse electric (TE) set with components E_z, B_x, B_y, and transverse magnetic (TM) set with components E_x, E_y, B_z. These sets are uncoupled. In Appendix A we prove that only one boundary condition is needed for each set, such as E_z and B_z, and the other components can be obtained from the Maxwell equation. However, TM field components E_x and E_y depend on the current density components j_x and j_y which are unknown at the boundary. An alternative is to give the conditions on E_x, E_y, instead of those on B_z, j_x and j_y. Actually, only E_x at the top and bottom boundaries or E_y at the left and right boundaries is necessarily required for solving the Maxwell equations (see Appendix A). The other conditions are given so as to solve the particle motion equations.

Thus, the boundary conditions for field quantities are taken as

$$E_x = 0, \quad \frac{\partial E_y}{\partial y} = 0, \quad E_z = E_{zd}(x,t), \quad \text{at } y = \pm y_b, \tag{2.32}$$

$$\frac{\partial E_x}{\partial x} = \frac{\partial E_y}{\partial x} = 0, \quad \frac{\partial E_z}{\partial x} \text{ continuous}, \quad \text{at } x = \pm x_b, \tag{2.33}$$

where E_{zd} is the external driving electric field. The choice of boundary conditions is required to ensure that the system can transit to a steady state.

2.3.2 Particle quantities

The upstream boundary is set in the ideal MHD region where both electrons and ions are frozen in the magnetic field. Thus the plasma inflow is symmetrically supplied with the $\mathbf{E} \times \mathbf{B}$ drift velocity from two upstream boundaries into the simulation domain. The input particle distribution is given by a shifted Maxwellian with the initial constant temperature (T_{s0}), where the average velocity $\mathbf{u}_d$ and density n_d are

$$\mathbf{u}_d = \frac{\mathbf{E}_d \times \mathbf{B}_d}{B_d^2}, \tag{2.34}$$

$$n_d = n_{d0} \frac{B_d}{B_{d0}}, \tag{2.35}$$

where subscript d stands for the upstream boundary and subscript 0 for the initial time. The corresponding input particle flux is proportional to E_{zd} as

$$n_d u_{yd} \propto E_{zd}. \tag{2.36}$$

An open downstream boundary means that particles can not only go out of but also come into the system across it, which is illustrated in Fig. 2.2. The outgoing particles can be obtained directly by observing the motion of particles at the boundary. The questions are how many particles go into the system, and how to assign the positions and velocities of these incoming particles. To determine the incoming particle numbers we choose a region I with width of five grids ($5\Delta x$) on the boundary and calculate the average particle velocity $\langle v_x \rangle$ in this region. Then we obtain the net number of outgoing particles passing across the boundary during one time step Δt as

$$N^{net} = -n\langle v_x \rangle \Delta t \cdot 2y_b \tag{2.37}$$

where n is the average particle number density in region I. According to the charge neutrality condition, the net numbers for electrons and ions are the same. So the numbers of incoming electrons and ions are given as

$$N_e^{in} = N_e^{out} - N^{net}, \quad N_i^{in} = N_i^{out} - N^{net}. \tag{2.38}$$

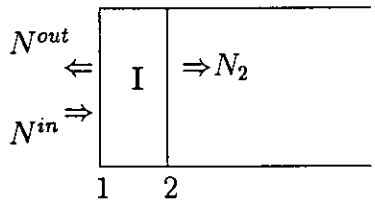

Figure 2.3: Illustration of the free boundary condition for particles.

As the next step, we have to assign the positions and the velocities of the incoming particles. We assume that the physical state outside is the same as that in region I, to say, the particle distribution function outside is the same as that in region I. Thus, the positions and velocities of the incoming particles can be defined by using the information of particles crossing surface 2 from left to right in Fig. 2.3. For example, if $N_e^{in} \leq N_{e2}$, the information of N_e^{in} particles randomly selected among N_{e2} particles crossing surface 2 is copied to the incoming electrons; if $N_e^{in} \geq N_{e2}$, then $N_e^{in} - N_{e2}$ outgoing particles are randomly selected and then reflected except for u_{ex}^{in} which obeys $u_{ex}^{in} = -u_{ex}^{out} + 2\langle v_x \rangle$ so as to satisfy the condition $u_{ex}^{in} > 0$. Since $|1 - N_{e2}/N_e^{in}| \ll 1$, this treatment seems not bad.

2.4 Initial condition

The simulation begins with a Harris-type equilibrium [60] as

$$B_x(y) = B_0 \tanh(y/L), \tag{2.39}$$

$$P(y) = (B_0^2/8\pi)\,\mathrm{sech}^2(y/L), \tag{2.40}$$

$$j_z(y) = -(cB_0/4\pi L)\,\mathrm{sech}^2(y/L), \tag{2.41}$$

where B_0 is a constant and L is the scale height along the y-axis. The magnetically neutral sheet is on the x axis ($y = 0$). The electric field vanishes initially because both ions and electrons are loaded to the same spatial positions.

The electron and ion distribution functions are the shifted Maxwellian as

$$f_s(v_x, v_y, v_z) = n(y)\left(\frac{m_s}{2\pi T_{s0}}\right)^{3/2} \exp\left\{-\frac{m_s}{2T_{s0}}\left[v_x^2 + v_y^2 + (v_z - u_{s0})^2\right]\right\}, \tag{2.42}$$

$$n(y) = \frac{B_0^2}{8\pi(T_{e0} + T_{i0})}\,\mathrm{sech}^2(y/L), \tag{2.43}$$

$$u_{s0} = -2cT_{s0}/q_s B_0 L. \tag{2.44}$$

The constants u_{s0} and T_{s0} represent the diamagnetic drift velocity and the temperature of particles of species s, respectively. It is seen that in the Harris equilibrium the magnetic field confining the plasma is maintained by the diamagnetic current.

Chapter 3

Overview of Simulation Results

3.1 Simulation parameters

The simulation is carried out on a 512×128 point grid by using 6.4 million particles. The simulation box with a big aspect ratio, $x_b/y_b = 6$, is used so as to reduce the effect of the numerical noises excited at the downstream boundary on the reconnection. The main parameters are in the following: the mass ratio of ion to electron $m_i/m_e = 25$, the charge ratio $q_i/q_e = 1$, $T_{i0}/T_{e0} = 1$, $\omega_{pe0}/\omega_{ce0} = 3.5$, $L = 0.8y_b \approx 3\rho_{i0}$, where ω_{pe0} is the plasma frequency associated with the density on the neutral line, ω_{ce0} is the electron cyclotron frequency associated with B_0, and ρ_{i0} is the ion Larmor radius. Thus, $x_b \approx 22\rho_{i0}$ and $y_b \approx 3.66\rho_{i0}$. The relations $L > \rho_{i0} > c/\omega_{pe0} > \Delta y$ hold in the initial configuration, where Δy $(= \lambda_{d0})$ is the grid separation along the y-axis and λ_{d0} $(= v_{te0}/\omega_{pe0})$ is the Debye length. The above relations assure the size of dissipation region to be smaller than that of the system in the y direction when reconnection takes place. The time step is chosen as $\omega_{ce0}\Delta t = 0.02$ from the CFL condition.

The input rates of mass flux and the magnetic flux are uniquely determined by an out-of-plane electric field imposed at the upstream boundary where both electrons and ions are magnetized. The driving electric field $E_{zd}(x,t)$ is shown in Figure 3.1: (a) the temporal change at x=0, (b) the spatial profiles at the five marked times in panel (a). The field E_{zd} is set for zero at $t = 0$ and gradually increases predominantly in a region with width of x_d in the early time, and then develops on the whole boundary until it reaches a constant value E_0. After $\omega_{ci0}t = 5.72$, E_{zd} keeps a constant value E_0 which is a necessary condition for a reconnection system to evolves toward a steady state. Hence the characteristic feature of $E_{zd}(x,t)$ is determined by two parameters, i.e., the non-uniformity scale x_d in the early phase and the value of the uniform field E_0. It is worthwhile to note that, although E_{zd} is uniform in the later time, the magnetic field is always non-uniform at the upstream boundary. Furthermore, it depends strongly on x_d and can change with time. According to Faraday's law the y-component of magnetic field at the upstream

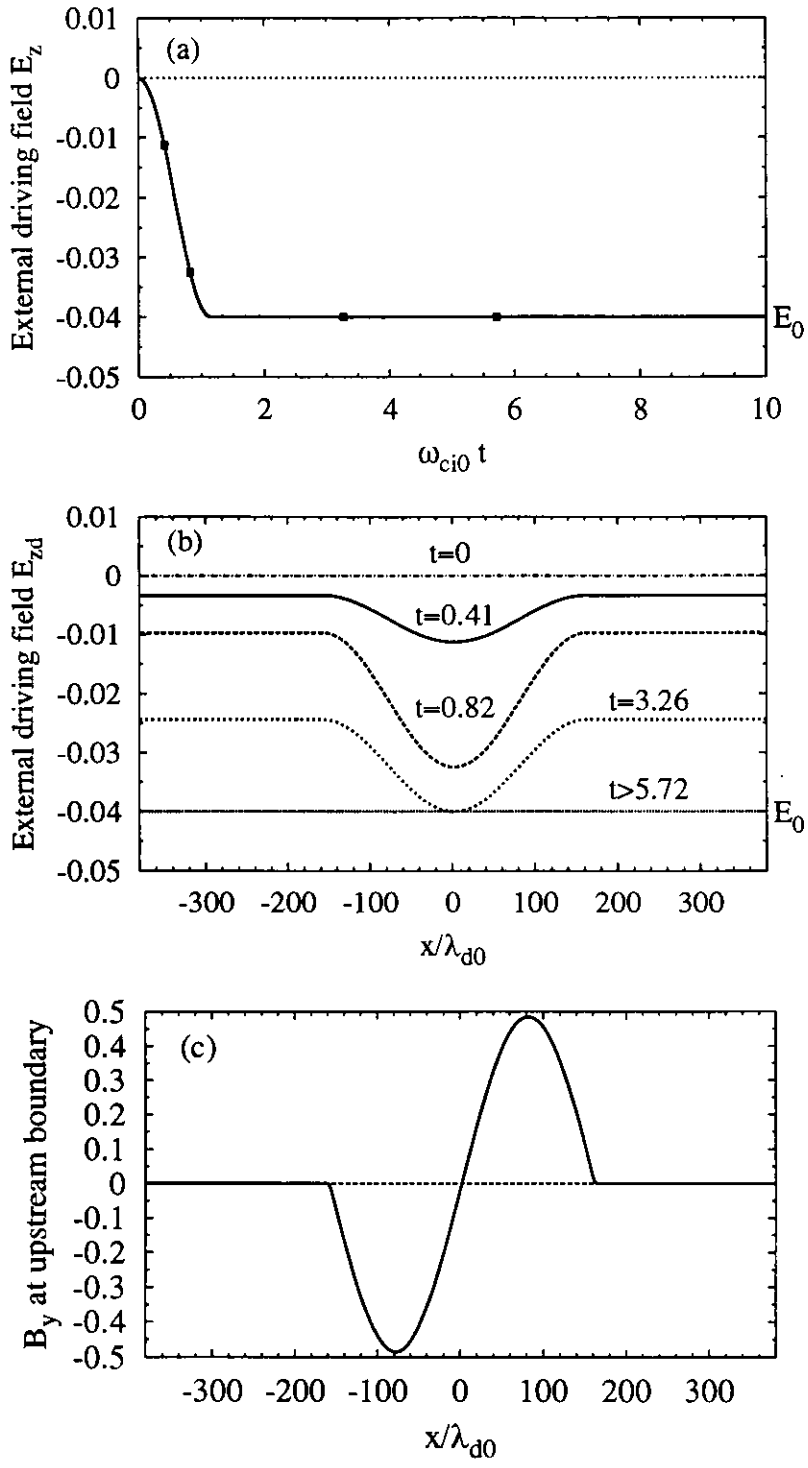

Figure 3.1: The external driving electric field $E_{zd}(x,t)$: (a) the temporal change at the center ($x = 0$) of the upstream boundary, (b) the spatial profiles at the marked times in panel (a). (c) shows the profile of y component of the corresponding boundary magnetic field after E_{zd} becomes constant ($\omega_{ci0}t > 5.72$).

boundary, B_{yd}, has the form as

$$B_{yd}(x,t) \propto \frac{E_0}{x_d} \sin[\phi(x)], \tag{3.1}$$

$$\phi(x) = \begin{cases} -\pi, & x < -x_d \\ \pi x/x_d, & -x_d \le x \le x_d \\ \pi, & x > x_d. \end{cases} \tag{3.2}$$

at the late time of $\omega_{ci0}t > 5.72$, as shown in Fig. 3.1(c). The function form $\sin[\phi(x)]$ in the above expression comes from the fact that $E_{zd}(x,t) \propto \cos[\phi(x)]$ for $\omega_{ci0}t < 5.72$. It is seen from Fig. 3.1 and the relations (3.1) and (3.2) that the non-uniformity scale x_d actually affects the curvature radius of magnetic field lines at the upstream boundary, and thus the divergency of plasma inflow. Correspondingly, B_{xd} can be estimated from Ampere's law

$$\frac{\partial B_{xd}}{\partial y} \approx \frac{\partial B_{yd}}{\partial x} \tag{3.3}$$

where the current density is assumed to be approximately zero at the upstream boundary. This means that B_{xd} is not fixed but related to inner field structure. In other words, the boundary magnetic field can change with time so as to adjust the internal reconnection process.

3.2 Overview of simulation results

In order to study the dependence of the long-time scale reconnection process on the profile of driving electric field, we perform nine simulation runs with various sets of E_0 and x_d listed in Table 3.1. One of the important results of these runs is also summarized in this table.

We find that driven reconnection evolves in two ways. The system relaxes to a steady state with only one X point located at the center of the simulation domain for the small non-uniformity scale x_d. When the scale x_d increases to $0.83x_b$ the system behaves intermittently where magnetic islands are frequently formed to grow near the original X points. On the other hand, the evolution behavior is insensitive to the driving field strength E_0.

Simulation results in the steady state largely help us to understand physical mechanism of collisionless driven reconnection. In the following chapter, we will examine the features of steady reconnection with the focus on the electron dynamics and ion dynamics. After that, we will analyze the mechanism of intermittent phenomena and explore why the reconnection behavior in a long time scale is dependent on the scale x_d (equivalently, the pattern of driving flow) but independent of the flux input rate E_0.

Table 3.1: Driving field parameters and reconnection evolution behaviors

E_0/B_0 \ x_d/x_b	0.42	0.62	0.83
-0.04	**Steady** (Run 1)	**Steady** (Run 2)	**Intermittent** (Run 3)
-0.08	**Steady** (Run 4)	**Steady** (Run 5)	**Intermittent** (Run 6)
-0.08	**Steady** (Run 7)	**Steady** (Run 8)	**Intermittent** (Run 9)

Chapter 4

Steady Reconnection

Table 3.1 shows that the steady reconnection is realized for the runs of $x_d/x_b \leq 0.62$. For an openly driven system with appropriate boundary conditions steady reconnection is perfectly possible, and moreover comes true in our simulations. This fact implies that the numerical simulation gives us physically correct results with a high precision. In this chapter, we investigate the mechanism of steady magnetic reconnection based on the results of Run 1 with $x_d/x_b = 0.42$ and $E_0/B_0 = -0.04$.

4.1 Temporal evolution

Let us begin with describing the time evolution of magnetic reconnection. Figure 4.1 shows the temporal evolution of the magnetic field configuration, where ten panels represent the contours of magnetic flux A_z in x-y plane at different times. The top panel plots magnetic field in the initial Harris equilibrium configuration. The plasma inflow supplied from the top and bottom boundaries compresses the current sheet. Magnetic reconnection sets in at the center of the simulation domain at $\omega_{ci0}t = 4.9$. A magnetic island appears in the central region at $\omega_{ci0}t = 7.2$ and gradually moves to the right while increasing its spatial size. This island coalesces before it goes out of the system. From this time on no islands are created in the system and the global field topology remains unchanged. In other words, the system relaxes to a steady state.

Figure 4.2 shows (a) the evolution of the reconnection electric field E_r, (b) those of the electron and ion number densities and z-component current density $-j_z$, where all quantities are evaluated at the main X point if there are more than one X point. The reconnection electric field E_r, which is defined as the out-of-plane electric field at the X point, is a direct measure of the reconnection rate. Figure 4.2(a) shows that there are two temporal phases in the evolution of the reconnection, i.e., growing phase and saturation phase. The electric field begins to grow slowly as soon as both the plasma density and the current density increase in the current layer through the compression driven by the plasma

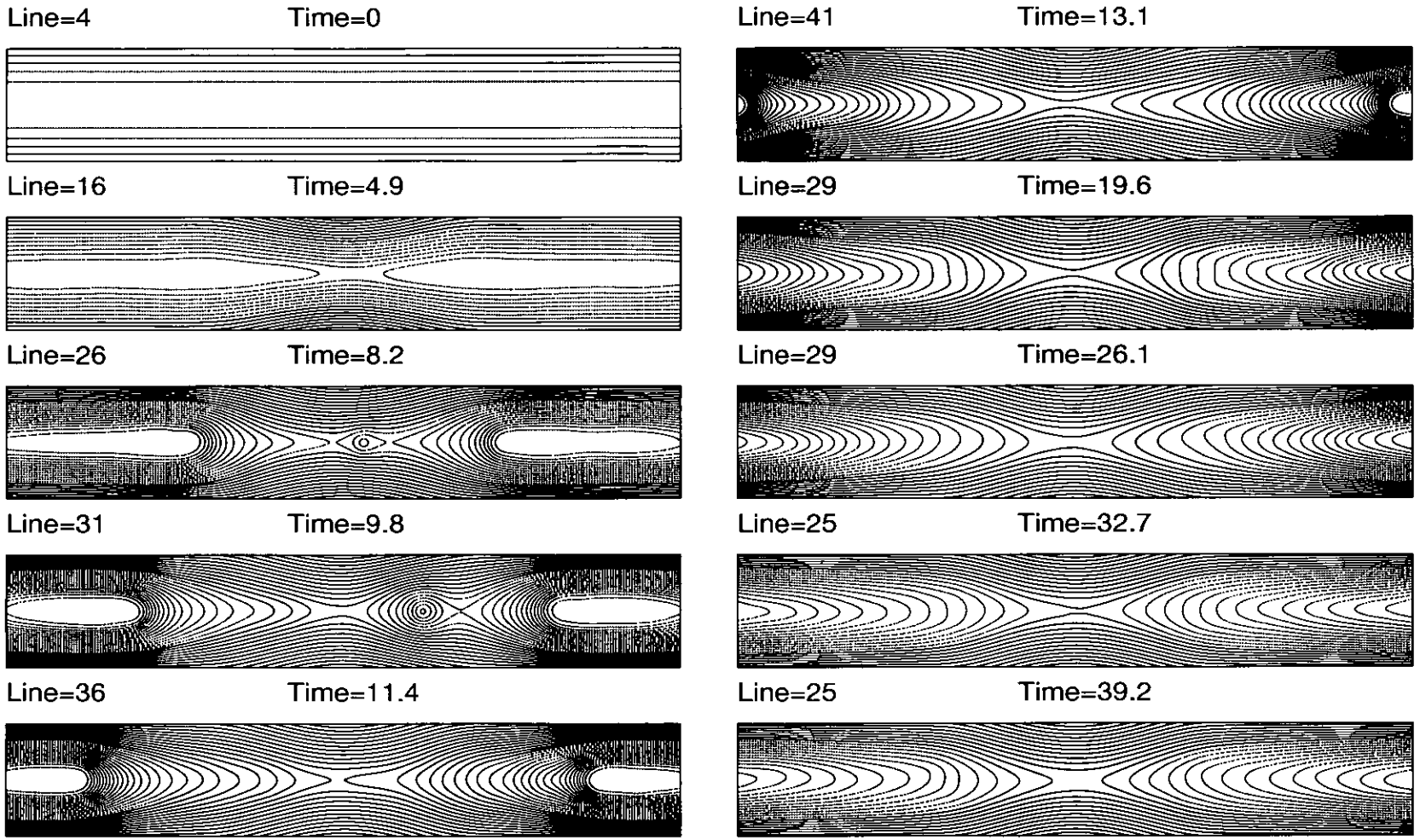

Figure 4.1: The temporal evolution of magnetic field configuration in the x-y plane for Run 1 where the time unit is ω_{ci0}^{-1}.

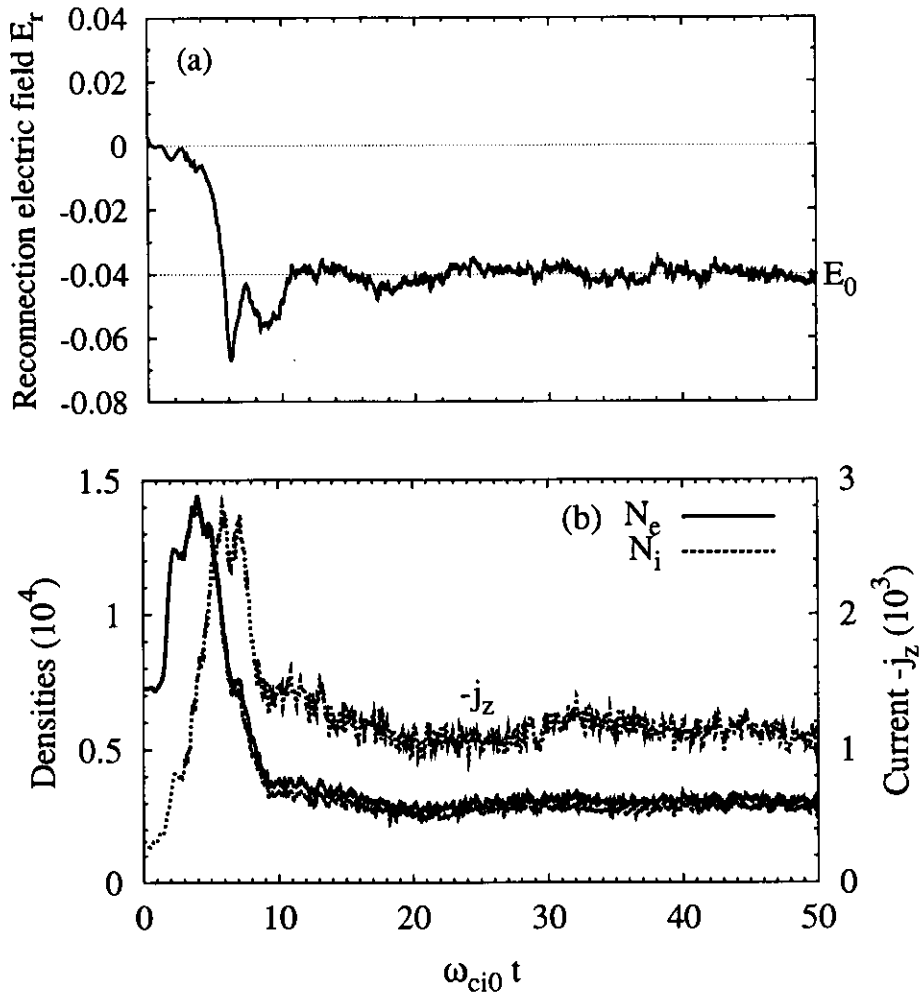

Figure 4.2: The histories of (a) reconnection electric field E_r, (b) the electron and ion densities and z-component current density $-j_z$ at the main X point for Run 1.

inflow from the upstream boundary. When the electron and ion densities are compressed to approach their peak values at $\omega_{ci0}t = 4.5$, an X-shaped magnetic separatrix becomes visible as a result of magnetic reconnection. Then the reconnection electric field rapidly grows up. Consequently, the generation of the outflow away from the X point causes the density decrease in the vicinity of the X point, while the current density continues to increase. Moreover, the electron density becomes a little dominant over the ion density due to the finite Larmor radius effect. When the densities drop below the initial value around $\omega_{ci0}t = 6$, the reconnection rate starts to saturate and so does the current density. After this period, E_r gradually approaches the value of the external driving electric field E_0, and the particle number densities and the current density relax to their own steady values, too. It is interesting to note that the density in the steady state is lower than the initial value. These results lead us to conclusion that the system transits to a steady

reconnection state in which the reconnection rate E_r is balanced with the flux input rate E_0 at the boundary. This conclusion is consistent with the requirement for a steady state. For 2D steady reconnection the out-of-plane electric field becomes uniform in space and constant in time, and therefore must be equal to the driving electric field E_0 at the upstream boundary, which is verified from Faraday's law.

Figure 4.3 shows the time histories of five spatial scales where the scales are calculated from the profiles in the y direction passing the X point and are normalized by the grid size λ_{d0}. The five curves represent half-width of current layer d_{jz}, electron meandering orbit amplitude l_{me}, ion meandering orbit amplitude l_{mi}, collisionless electron skin depth δ_e $(= c/\omega_{pe})$, and ion density scale d_h, respectively. The average meandering orbit amplitude of species s is given by [27, 28, 42]

$$l_{ms} = \sqrt{\delta \rho_s(\delta)}, \tag{4.1}$$

where $\delta = B_x/(\partial B_x/\partial y)$ is the magnetic field scale length, $\rho_s(y) = v_{ts}/\omega_{cs}$ the Larmor radius associated with $B_x(y)$ and $v_{ts} = \sqrt{T_s/m_s}$ the thermal velocity. Since B_x can be approximated as a linear function of y near the reconnection point, Eq. (4.1) becomes

$$l_{ms} = \rho_s(l_{ms}), \tag{4.2}$$

that is, the average meandering orbit amplitude is equal to the local Larmor radius [31]. Considering nonuniform temperature profile, we here define the meandering orbit amplitude by using the solution of Eq. (4.2). The density scale d_h is defined as the half width for the case of single-peak profile of density or the half peak-to-peak distance for the case of two-peak profile. Comparing Fig. 4.3 with Fig. 4.1 one can find that the reconnection sets in when the current layer is compressed as thin as l_{mi} $(\omega_{ci0}t \approx 4.5)$. This implies that the reconnection is triggered by the thermal effect based on nongyrating ion motion. As the current layer is further compressed, the reconnection takes place more rapidly. When d_{jz} approaches l_{me} $(\omega_{ci0}t \approx 6)$, the reconnection field starts to saturate. As time goes on, however, d_{jz} gradually relaxes to l_{mi} again and the reconnection process gets steady with a constant rate.

Figure 4.3 also demonstrates another two features: (1) both d_{jz} and d_h almost change with the same rate at all times, and approach l_{mi} after the reconnection rate reaches maximum; and (2) δ_e is slight larger than l_{me} in the saturation phase. These features are fairly important for understanding the mechanism of magnetic reconnection. The first feature suggests that the structure of current layer is modified by the plasma density configuration which is controlled by massive ions although the electric current is carried predominantly by the electrons. The second feature implies two facts. One is that the electron frozen-in condition is broken mainly by the electron inertia effect. The other is the unity of electron orbit effect and electron inertia effect in electron dynamics.

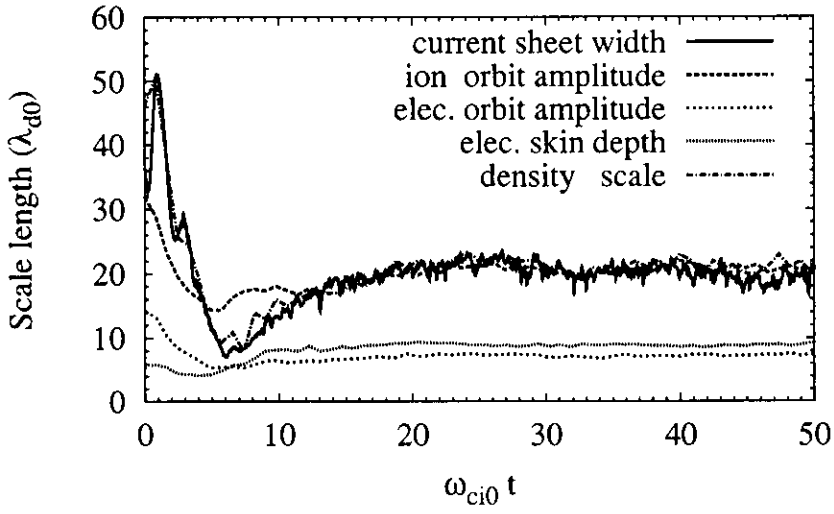

Figure 4.3: The temporal evolutions of five spatial scales, i.e., the half-width of current layer d_{jz}, the electron orbit amplitude l_{me}, the ion orbit amplitude l_{mi}, the electron skin depth δ_e, and ion density scale d_h, where the scales are calculated from the profiles in the y direction passing the X point and are normalized by λ_{d0}.

The features of reconnection in the growing phase exhibited in the present simulation is qualitatively in agreement with those of the previous periodic simulations [27, 28], which is not the focus of our attention. After reconnection field saturates, the system tends to a steady state and the current layer width relaxes to a scale of the ion meandering orbit size l_{mi} from the electron scale δ_e or l_{me}. This result clearly differs from that of non-driven reconnection in a closed system [36], in which the current layer width is scaled by the electron skin depth. The difference probably comes from the model used. In the recent experimental study [48] on the Magnetic Reconnection Experiment (MRX), the current layer width is found to be about $0.4c/\omega_{pi}$. This result is in good agreement with our simulation in which $d_{jz} \approx l_{mi} \approx 0.5c/\omega_{pi}$.

4.2 Spatial structure of physical quantities

In order to shed light on the physical mechanism of magnetic reconnection and the roles of electron dynamics and ion dynamics, we examine the spatial distribution of several physical quantities in the steady phase.

The vector plots of the electron and ion in-plane flow velocities at $\omega_{ci0}t = 39.2$ are shown in Fig. 4.4 where the profiles of their x components along the x-axis are also plotted in the bottom panel. The separatrix is also plotted with the dotted lines in the top and middle panels. The plasma inflows supplied through the top and bottom boundaries flow

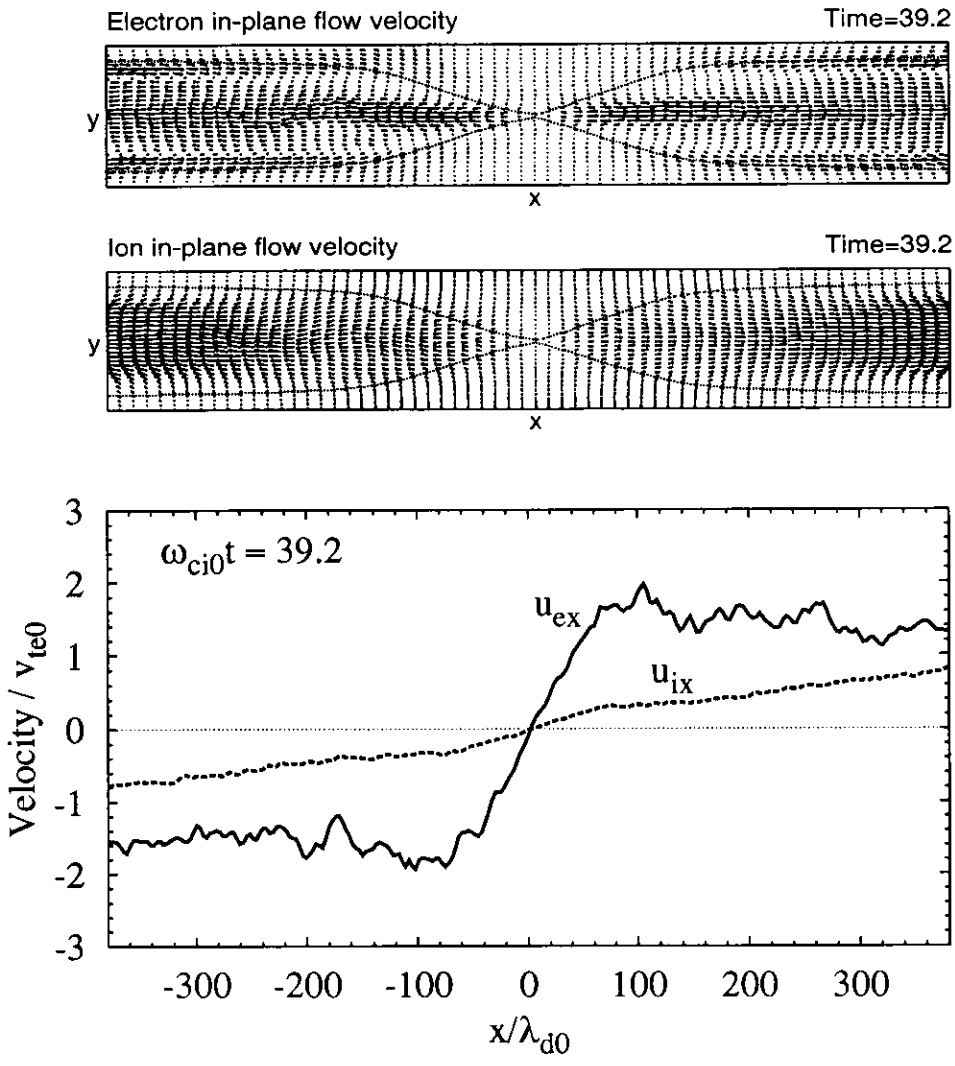

Figure 4.4: The in-plane flow velocities of electrons (top) and ions (middle), and the profiles of their x components along the x-axis (bottom) at $\omega_{ci0}t = 39.2$ for Run 1.

into the system. After moving across the separatrix ions turn and flow outward. The ion outflow velocity increases with the distance from the X point and is lower than the electron flow velocity in the whole downstream, which implies that the ions is unmagnetized. The electron flow pattern is quite different. In the vicinity of the separatrix there exists a distinct discontinuity which separates upstream from downstream. Some of upstream electrons cross the discontinuity into the downstream region. The others convergently flow toward the reconnection region along the magnetic field lines. A fast electron outflow is formed in the downstream region with width around $2l_{me}$ along the x axis ($y = 0$), which is much more localized than that of ions. The outflowing velocity reaches its peak value at a distance about $0.2x_b$ ($\approx 80\lambda_{d0}$) from the X point. This picture implies that the dissipation region scales of electrons and ions are different.

Figure 4.5 shows (a) the colored perspective view of the ion out-of-plane flow velocity $-u_{iz}$, (b) that of electron out-of-plane flow velocity u_{ez}, and (c) that of current density $-j_z$ in the x-y plane at $\omega_{ci0}t = 39.2$, where the blue and red respectively denotes the low and high values and the scales are different for different figure for the resolution of details of interest (hereafter). The value of $|u_{ez}|$ is larger than $|u_{iz}|$ almost everywhere. Especially, the difference becomes much significant in the vicinity of the X point. The ion out-of-plane flow exhibits a two-peak structure in which the peak-to-peak distance is about $2l_{mi}$ in the region of $|x| < 0.3x_b$ ($\approx 115\lambda_{d0}$) and a little wider outside. The electron out-of-plane flow is peaked around the x axis ($y = 0$) with the half width slight wider than δ_e in $|x| < 0.3x_b$. The flow pattern is split into fours peaks in $0.3x_b < |x| < 0.4x_b$ and then develops a three peak structure in $|x| > 0.4x_b$ ($\approx 150\lambda_{d0}$). Figure 4.5(d) shows the positions of the discontinuity (y_d) which is estimated with the position of $u_{ex} = 0$, peak of u_{iz} (y_{iz}) and outer peak of u_{ez} (y_{ez}), and ion meandering orbit amplitude l_{mi} along the x axis, where l_{mi} is estimated by using the x-component of magnetic field B_x. It is clear that the peak-to-peak distance of u_{iz} is about $2l_{mi}$ in the reconnection region and as $|x|$ increases it becomes slight wider and then approaches $2l_{mi}$ again at the downstream boundary. The outer peaks of u_{ez} are very close to the discontinuities. It is noteworthy from Fig. 4.5(c) that due to the modulation of the plasma density distribution the current layer has the width of about $2l_{mi}$ around the X point but its maxima are at both downstream boundaries.

The spatial distribution of electron number density at $\omega_{ci0}t = 39.2$ is plotted in Fig. 4.6(a). It is evidently seen that there exists a low density channel along the x-axis ($y = 0$) over the wide range from the X point to the downstream boundary. The width of the channel, the peak-to-peak distances of density profile, is $2l_{mi}$ in the whole region as shown in Fig. 4.6(b). The fact that the spatial structure of electron density is of ion orbit scale l_{mi} implies that the plasma density is controlled by ion motion through the electrostatic interaction between ions and electrons.

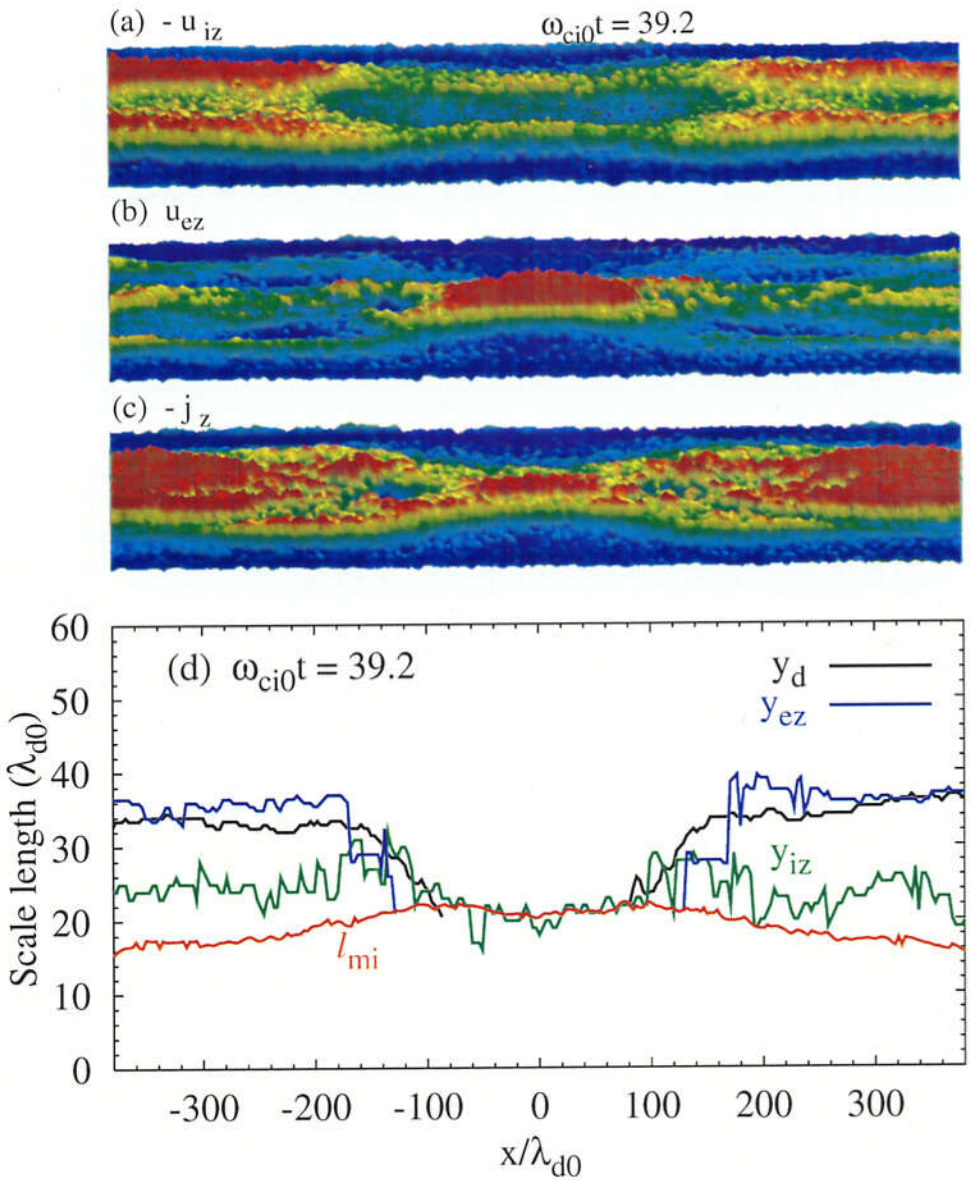

Figure 4.5: The perspective view of the out-of-plane components of (a) ion flow velocity $-u_{iz}$, (b) electron flow velocity u_{ez}, and (c) current density $-j_z$ in the x-y plane; and (d) the positions of the discontinuity (y_d), peak u_{iz} (y_{iz}) and outer peak u_{ez} (y_{ez}), and ion meandering orbit amplitude l_{mi} along the x axis.

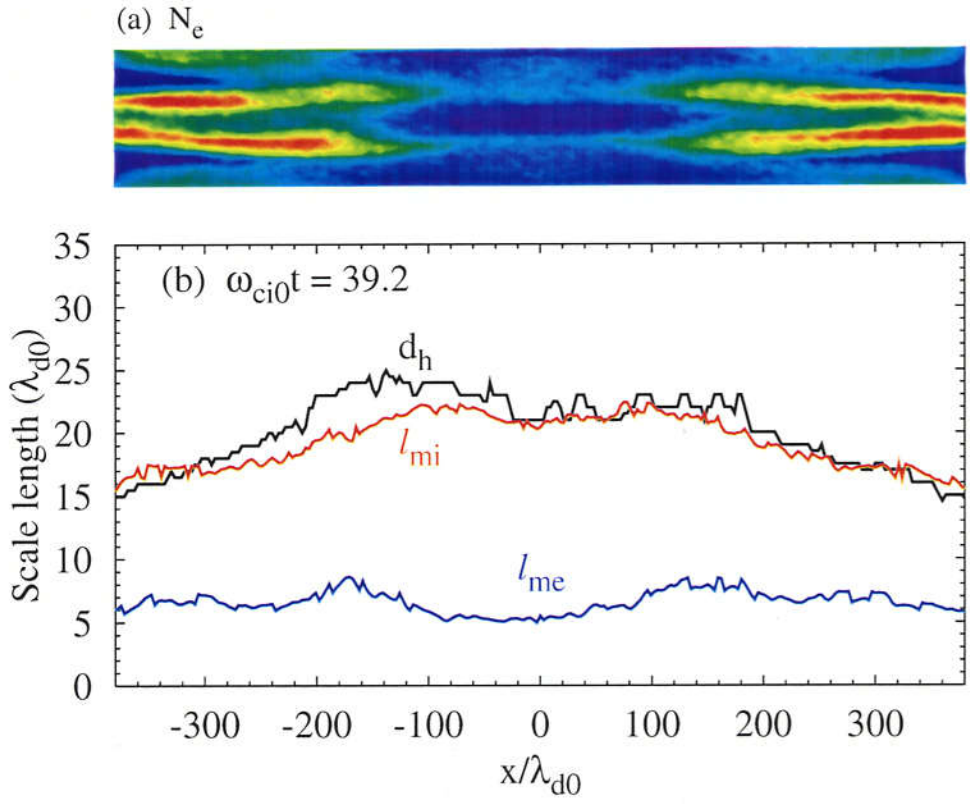

Figure 4.6: (a) The perspective view of electron density in the x-y plane, and (b) the half width of low-density channel and the electron and ion meandering orbit amplitude radii versus x.

Figure 4.7 shows the perspective view of (a) ion temperature and (b) electron temperature in the x-y plane at $\omega_{ci0}t = 39.2$. Their profiles along the vertical lines across the X point ($x = x_r$) and along $x = 261\lambda_{d0}$ ($\approx 0.68x_b$) are plotted in Fig. 4.7(c) and (d), respectively. It is evident that the inflow ions experience heating twice, i.e., the first is near $|y| \approx 2l_{mi} \approx 40\lambda_{d0}$ and the second in the region of l_{mi}. Thus the ion temperature T_i is strongly peaked around the x-axis with width of $2l_{mi}$. In contrast, the electron temperature T_e is almost unchanged in the region of $|x| < 0.2x_b$. The electron heating only takes place both in the range of $0.2x_b < |x| < 0.4x_b$ along the x-axis and near the discontinuity. T_e keeps constant in the downstream region of $|x| > 0.4x_b$. It is noted that the ion temperature is much higher than the electron one. This result is in agreement with the experimental observation in MRX [48, 49] which indicates strong non-classical ion heating in a 2D reconnection layer with ion scale. The anomalous ion heating has also been observed in 3D magnetic reconnection experiment in TS-3 [50].

Let us examine where the frozen-in constraint, $\mathbf{E} + (\mathbf{u}_s/\mathbf{c}) \times \mathbf{B} \approx \mathbf{0}$, is broken. Figure 4.8 (a) shows the spatial profiles of E_y, $-u_{ez}B_x/c$ and $-u_{iz}B_x/c$ along the vertical line passing the X point at $\omega_{ci0}t = 37.6$. In order to resolve the structure in electron scale we

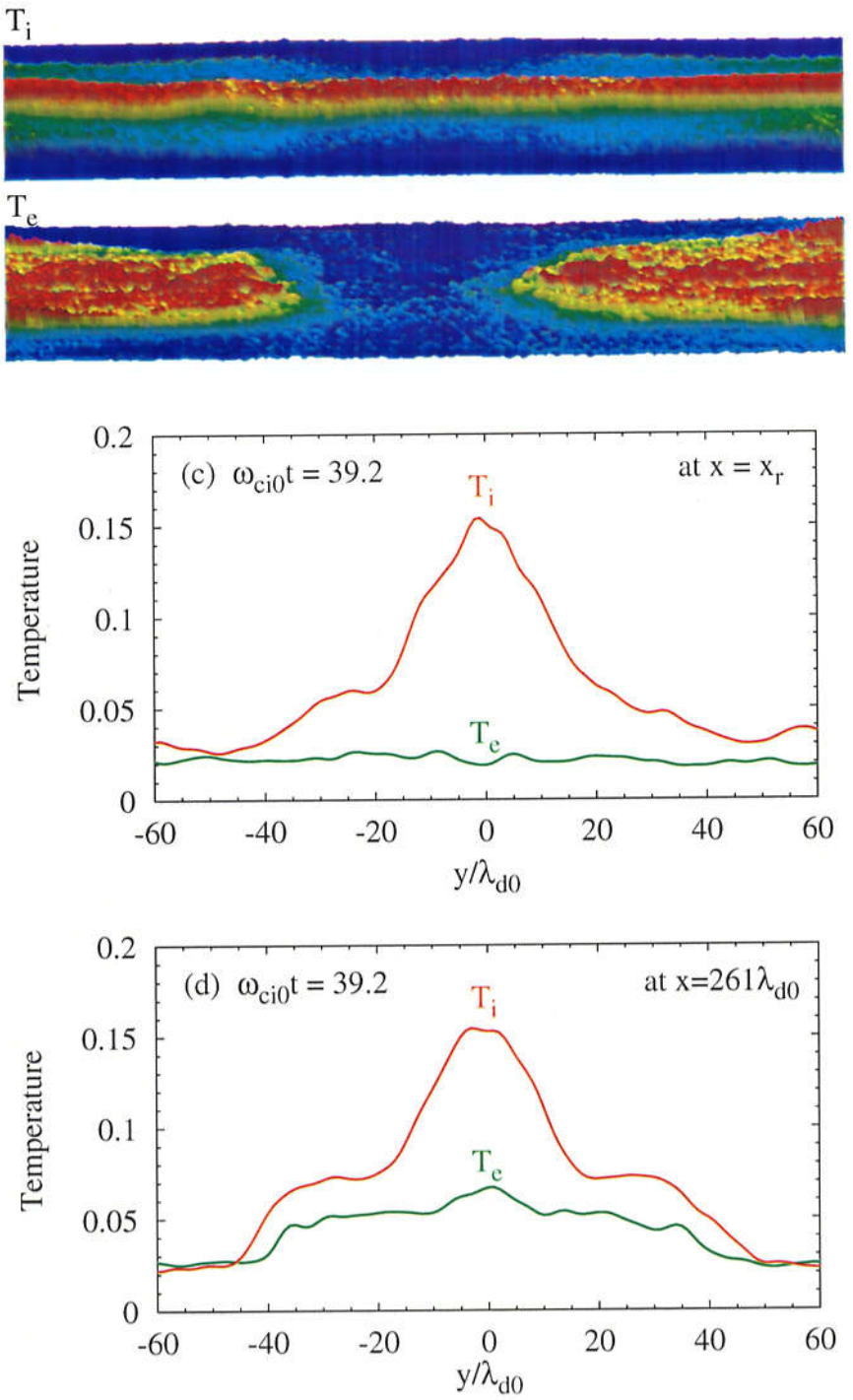

Figure 4.7: The perspective view of (a) ion temperature and (b) electron temperature in the x-y plane at $\omega_{ci0}t = 39.2$, and their vertical profiles (c) across the X point and (d) along $x = 261\lambda_{d0}$.

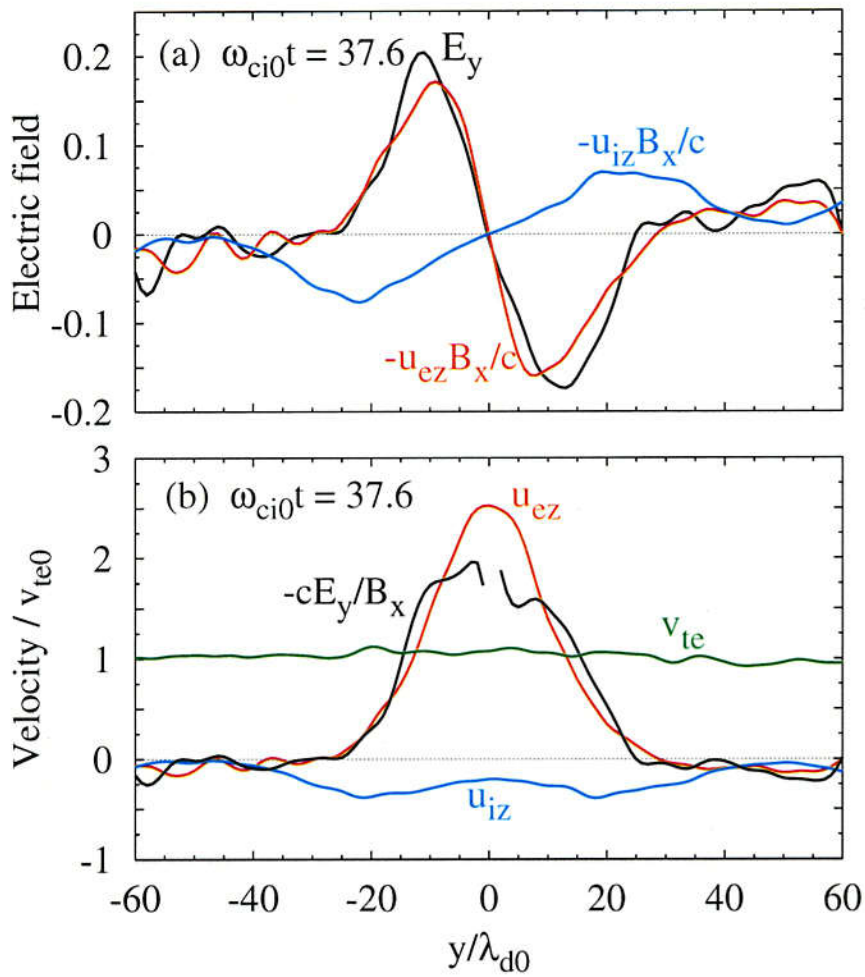

Figure 4.8: The profiles along $x = x_r$ of (a) E_y, $-u_{ez}B_x/c$ and $-u_{iz}B_x/c$, and (b) u_{ez}, u_{iz}, $-cE_y/B_z$ and v_{te} at $\omega_{ci0}t = 37.6$.

plot the profiles of u_{ez}, u_{iz}, the electric drift velocity cE_y/B_x and the electron thermal velocity v_{te} in Fig. 4.8(b) by using the same data as Fig. 4.8(a). It is evident that the ion motion decouples from the magnetic field within a region of $|y| \leq c/\omega_{pi}$ ($\simeq 40\lambda_{d0} \simeq 2l_{mi}$) while the electrons remain frozen in the magnetic field until they enter a region of scale δ_e.

The observation of fluid quantities suggests that the dissipation region in the steady phase is of a two-scale structure underlying the quite different characteristics scale lengths of electron dynamics and ion dynamics. The inner electron dissipation region is $2l_{me}$ wide and $2 \times 0.4x_b$ ($\approx 2x_d$) long. The ion dissipation region is $2c/\omega_{pi}$ ($\simeq 2l_{mi}$) wide and the length is of the order of system length $2x_b$. Although the decoupling of ions from magnetic field is due to the inertia effect, the ion meandering motion plays an important role in ion dynamics, which controls the spatial structures of ion quantities with the scale l_{mi}. The fact that the density channel, the ion temperature peak and the two-peak u_{iz} with the

width $2l_{mi}$ stretch to the downstream boundary manifests that the ions are unmagnetized in the whole downstream. That is, the length of ion dissipation region is longer than the system size $2x_b$.

4.3 Mechanism of steady reconnection

4.3.1 Ion dynamics

As ions are driven into the ion dissipation region, they become unmagnetized due to the inertia effect while the electrons remain frozen in the magnetic field until they enter a region of scale δ_e. This phenomenon is caused by the Hall term, as was seen in Eqs. (1.6)-(1.7). An electrostatic field E_y is thus generated as a result of the decoupling of electron motion and ion motion [see Fig. 4.8(a)]. This electric field accelerates the ions to follow the electrons which move inwards at the increasing drift velocity cE_z/B_x. Meanwhile, the ions are also accelerated in -z direction by the electric field E_z. After crossing the neutral line, the ions are decelerated in y direction by E_y and v_zB_x/c forces while they remain accelerated in -z direction by E_z. Under the combined action of the magnetic field B_x and electric fields E_y and E_z, the ions bounce back and forth across the x-axis in y direction, i.e., meandering motion. One of typical ion meandering orbits in the y-z plane is illustrated in Fig. 4.9. It is noteworthy from Fig. 4.8(a) that the electrostatic field E_y has the same direction as v_zB_x/c and dominates over it. The bounce motion of ions is intensified due to this character. Both the bounce frequency and bounce energy are greatly increased as ions bounce. Consequently, the velocity $|v_y|$ becomes maximum at the x-axis, while the $|v_z|$ becomes maximum at its turning point. The minimum of $|v_z|$ also appears at the x-axis since $-v_yB_x/c > |E_z|$ when the ion moves toward the neutral line.

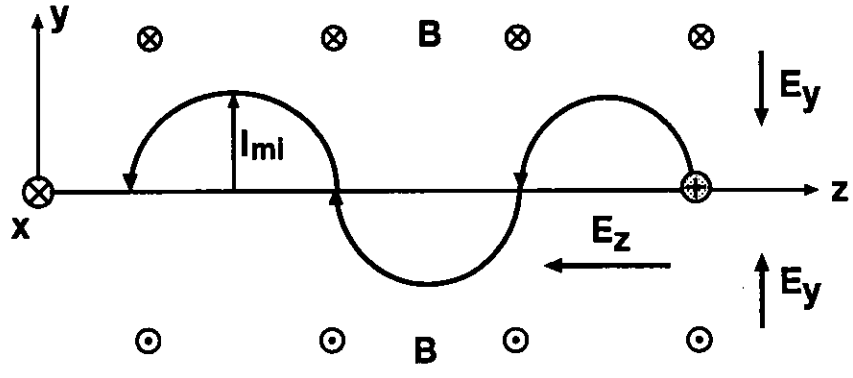

Figure 4.9: The illustration of one of the typical ion meandering orbits.

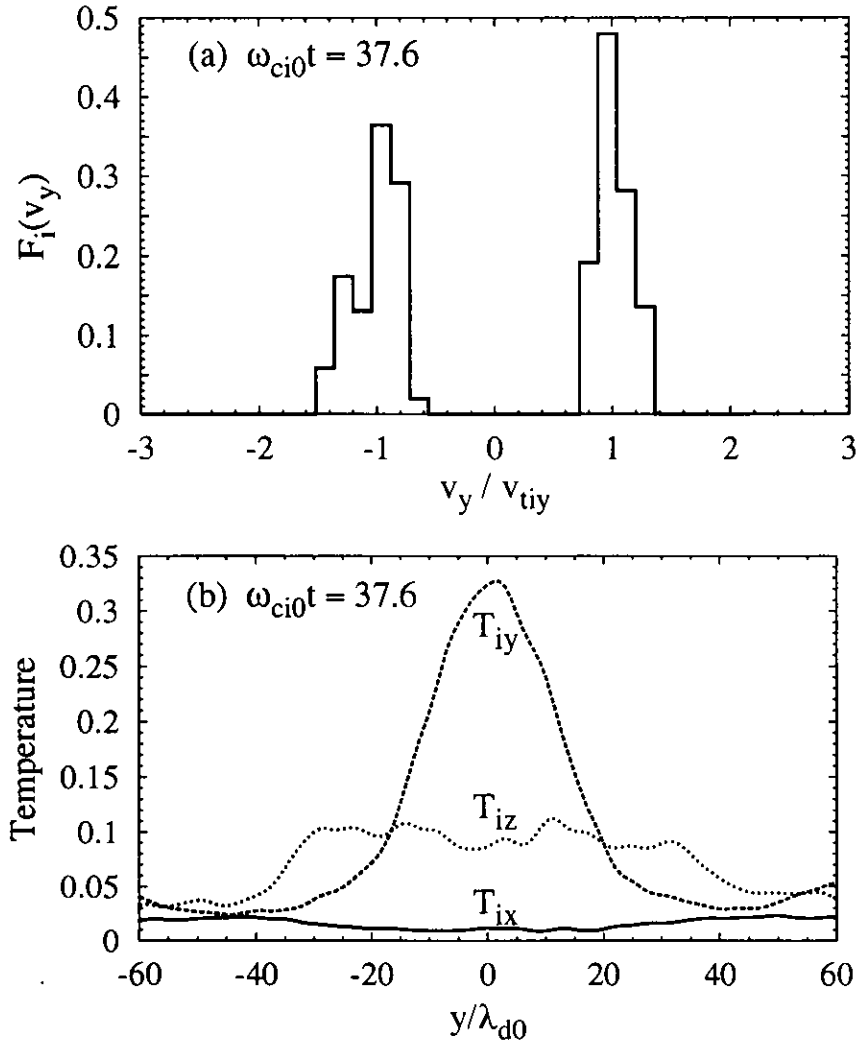

Figure 4.10: (a) The ion velocity distribution function $f(v_{iy})$ at the X point, and (b) the profiles of the ion temperatures T_{ix}, T_{iy} and T_{iz} in three directions along $x = x_r$.

A number of ions flow into the low magnetic field region from the upstream region on both sides and perform the meandering motion until they are ejected out toward the downstream. Therefore, we expect that the z-component of the ion flow velocity u_{iz} exhibits a bimodal structure on both sides of the x-axis, and that the ion velocity distribution function at the X point exhibits two counterstreaming components in v_{iy} space. Figure 4.5(a) shows the double peaks appear at $y = \pm l_{mi}$ in the profile of ion flow velocity u_{iz}, as expected. The peak position implies that the average orbit amplitude of ion meandering motion is l_{mi}. Figure 4.10(a) shows the ion velocity distribution function $f(v_{iy})$ at the X point where v_{iy} is normalized by $v_{tiy} = \sqrt{T_{iy}/m_i}$ and $T_{iy} = m_i\langle(v_{iy} - u_{iy})^2\rangle$ is the ion temperature in the y direction. The function $f(v_{iy})$ consists of two counterstreaming beams, which is consistent with our expectation. Similar results were

presented in the hybrid simulations of magnetic reconnection [35]. This picture implies that the thermal effect is associated with the bounce motion since the average velocity u_{iy} is almost zero at the X point. Figure 10(b) shows the spatial profiles of of ion temperatures in three directions, T_{ix}, T_{iy} and T_{iz}, along the vertical line passing the X point. The temperature T_{iy} in y-direction is much higher than those in the other directions in the region of $2l_{mi}$. This is due to the action of the electrostatic field E_y in the ion orbit motion. Therefore, the ion meandering motion plays an important role in the ion heating in the ion dissipation region shown in Fig. 4.7(a) and (c), and the formation of bimodal structure in ion out-of-plane flow velocity in Fig. 4.5(a).

The formation of the low-density channel with the width of $2l_{mi}$ is due to the the ion meandering motion, too. The transit time for a bouncing (or meandering) ion passing the same distance in y direction is longer near the turning point than near the neutral line. The difference of the transit times directly results in the density difference at two points. That is, the ion density at turning point is larger than at the neutral line. This is the reason why the density channel can be formed in this region shown in Fig. 4.6. The same mechanism explains ion depletion in the channel and accumulation at the density peak compared with the electron density distribution, i.e., the finite Larmor effect, which gives rise to the enhancement of electrostatic field E_y in the region between l_{mi} and l_{me} shown in Fig. 4.8(a). The maximum field strength of E_y is about five times as large as the reconnection electric field E_0.

According to the above discussion, there are two scale length in the ion dynamics: the ion skin depth $c/\omega_{pi} \simeq 40\lambda_{d0}$ corresponding to the ion inertia effect, and the meandering orbit size $l_{mi} \simeq 20\lambda_{d0}$ to the ion thermal effect. Although ions start to decouple from the magnetic field within a region of the scale c/ω_{pi} due to ion inertia effect as shown in Fig. 4.8, the ion dynamics is dominantly controlled by the ion meandering motion because the ions perform the meandering motion much longer. Remember that the ion out-of-plane flow u_{iz}, density and ion temperature T_i all exhibit the ion orbit scale l_{mi} in the whole system along the x-axis (see Figs. 4.5-4.7).

4.3.2 Electron dynamics

When electrons are driven into the ion dissipation region of scale $c/\omega_{pi} \simeq 40\lambda_{d0}$ by $\mathbf{E} \times \mathbf{B}$ drift, they feel the electrostatic field E_y due to the decoupling from the ion motion shown in Fig. 4.8(a). In contract to the unmagnetized ions, the electrons are not decelerated in the inflow direction by E_y but essentially perform a drift motion with the velocity $-cE_y/B_x$ in the out-of-plane direction. Therefore, the electron flow gets a high velocity in the z direction before entering its dissipation region. Since the current is carried predominantly by the electrons and $\partial/\partial y \gg \partial/\partial x$, we have the following estimate for the electron flow

velocity:

$$u_{ez} \approx \frac{j_z}{n_e e} \approx \frac{c}{4\pi n_e e}\frac{\partial B_x}{\partial y}. \tag{4.3}$$

Assuming that $\partial B_x/\partial y \approx B_x(\delta)/\delta$ with the width of the electron dissipation region δ, Eq. (4.3) becomes

$$u_{ez}(\delta) \approx \frac{\delta_e^2}{\delta}\omega_{ce}(\delta) \approx \left(\frac{\delta_e}{l_{me}}\right)^2 v_{te} \tag{4.4}$$

where l_{me} is the amplitude of electron meandering orbit defined by Eq. (4.1). It is seen that $u_{ez} > v_{te}$ if $\delta = \delta_e > l_{me}$, which is consistent with our simulation result shown in Fig. 4.8(b).

The fact that δ_e is slightly wider than l_{me} shown in Fig. 4.3 implies that the electron inertia effect is mainly responsible for breaking down the electron frozen-in condition in steady magnetic reconnection. Nevertheless, the thermal effect based on the meandering orbit can not be ignored because it is important in balancing the reconnection electric field in the vicinity of the X point where the inertia term vanishes according to Eq. (1.4) [27, 28, 29, 30, 31].

The role of electron inertia effect can be explained as follows. Assuming that the zeroth-order velocity of the electron flow entering the dissipation region is equal to $u_{ey0} = cE_z/B_x$ in the y direction and $u_{ez0} = -cE_y/B_x$ in the z direction, we can estimate the first-order correction due to the inertia term in a steady state as follows

$$u_{ey1} = \frac{mc}{eB_x}u_{ey0}\frac{\partial u_{ez0}}{\partial y}, \tag{4.5}$$

$$u_{ez1} = -\frac{mc}{eB_x}u_{ey0}\frac{\partial u_{ey0}}{\partial y}, \tag{4.6}$$

where the pressure term is ignored. Note that the inertia correction u_{ey1} gives rise to the reduction of velocity in the y direction because u_{ey1} has an opposite sign to u_{ey0}. Using Eq. (4.3) in place of u_{ez0}, we obtain

$$\frac{u_{ey1}}{u_{ey0}} = \delta_e^2\frac{1}{B_x}\frac{\partial^2 B_x}{\partial y^2}, \tag{4.7}$$

where the density variation is assumed to be negligibly small in the electron scale. It is clear that the violation of the frozen-in condition for electrons takes place due to the inertia effect in the region $|y| \leq \delta_e$ where $u_{ey1} \sim u_{ey0}$. The result leads to a rapid decrease in u_{ey} and thus a rapid increase in u_{ez} because $B_x^{-1}(\partial u_{ez0}/\partial y) < 0$. The physical role of E_y field can also be explained by using the analogy to the polarization drift of a particle in a time varying electric field. Consider an electron in the presence of B_x and E_y. There is only an $\mathbf{E} \times \mathbf{B}$ drift in the z direction. If there is another electric field component E_z, the electron moves at the drift velocity cE_z/B_x in the y direction. Because of E_y varying with y, the electron moving in the y direction feels as if E_y changed with time. Thus, due

to inertia the electron is further forced to perform a "polarization drift" in the y direction as

$$u_p = -\frac{c}{\omega_{ce}}\frac{d}{dt}\left(\frac{E_y}{B_x}\right) = -\frac{1}{\omega_{ce}}\frac{cE_z}{B_x}\frac{\partial}{\partial y}\left(\frac{cE_y}{B_x}\right), \tag{4.8}$$

which gives the same result as Eq. (4.5). Therefore, the electrostatic field E_y plays an important role in the electron inertia effect.

The electrostatic field E_y also plays a role in the electron meandering motion along the y direction in the electron dissipation region, which is different from that in the ion motion. The field E_y cancels out some part of restoring force $v_{ez}B_x/c$ for electron bounce motion along y because E_y has an opposite sign to $v_{ez}B_x/c$, as shown in Fig. 4.8(a). This cancellation gives rise to great decrease both in the bounce frequency and in the bounce energy. Moreover, the high out-of-plane velocity v_{ez} of the electrons going into the region reduces the ejection time in the x direction acted by the force $v_{ez}B_y/c$. The ejection time is comparable with the bounce period in our simulation. Thus electron bounce motion in the y direction is not as important as in ion dynamics. This point is confirmed from Fig. 4.8(b) in which the electron out-of-plane flow velocity does not have the character of bounce motion (two-peak profile) with scale l_{me} as found in ion quantities. As a result, we can see from Fig. 4.7 that there is no significant increase in the average electron temperature. The energy obtained from the reconnection electric field is dominantly transformed into the kinetic energy in the x direction by ejection toward downstream region.

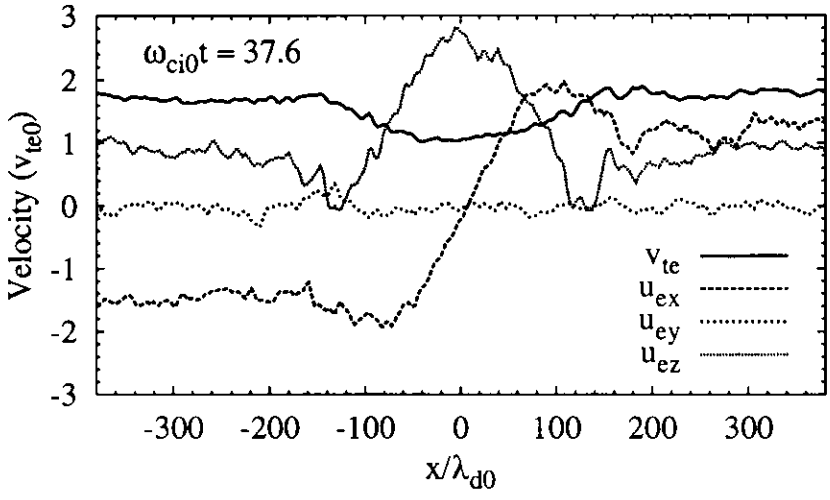

Figure 4.11: The profiles of thermal velocity v_{te} and three components u_{ex}, u_{ey} and u_{ez} of electron flow velocity along the x-axis.

Figure 4.11 shows the spatial profiles of electron thermal velocity and three components of electron flow velocity along the x-axis. The electron flow is accelerated in the z direction

near the X point by the reconnection field. As the electrons flow outward, the electron kinetic energy in the z direction is transformed to that in the x direction by $u_{ez}B_y/c$ force. After u_{ex} becomes maximum at $|x| = 0.2x_b$, electron flow is gradually decelerated and heated. When it approaches the edge of the electron dissipation region ($|x| = 0.4x_b$), u_{ex} becomes nearly equal to the thermal velocity and u_{ez} almost vanishes. Outside the electron dissipation region the electrons are re-frozen in the magnetic field, flowing outward at the velocity $-cE_z/B_y$, and thus the temperature keeps constant. The electron heating in the region of $0.2x_b < |x| < 0.4x_b$ results from the magnetization of electron motion. Consider a charged particle moving into a magnetized region from an unmagnetized region. It performs a gyration motion at its kinetic energy in a magnetized region, while its guiding center motion depends only on the drift processes, not on the velocity in the unmagnetized region. For a particle flow, the kinetic energy is converted into thermal energy by changing the particle motion to gyration motion when magnetized. Thus the electrons are heated through the magnetization process. This is the reason why the re-magnetized electron flow has thermal velocity just equal to the maximum value of its flow velocity u_{ex}.

4.3.3 Hall current structure

Now let us look at the reason why the upstream electrons convergently flow toward the reconnection region along the magnetic field lines (see Fig. 4.4). As electrons are driven toward the reconnection region along the vertical line passing the X point ($x = x_r$), the inflow flux increases with the flow velocity cE_z/B_x and the number density, which reaches maximum at the peak density. Obviously the input flux supplied from the input boundary is not enough to keep flux continuity without the flow convergence. Thus the depletion of the input flow flux requires a convergent electron inflow along the magnetic field lines. The force driving this inflow is related to an out-of-plane quadrupole magnetic field component B_z, which is shown in the top panel of Fig. 4.12. Due to the existence of B_z, the magnetic field vector is not in the x-y plane. The parallel component of electric field, mainly from E_z, to the magnetic field $\mathbf{B}$ drives electrons to flow along the magnetic field line, while the normal component makes electrons drift perpendicular to the field line in the plane. The field-aligned electron flow consists of the in-plane convergent inflow and out-of-plane flow. Similarly, the ions are accelerated in the opposite direction along the field line.

Because of different patterns between electron and ion in-plane flow velocities, an in-plane current structure is formed to sustain the out-of-plane magnetic field B_z, as shown in the bottom panel of Fig. 4.12, The in-plane current consists of the four current loops whose direction is outward in the upstream region and inward in the downstream region, which is sometimes called the Hall current system. The magnetic field B_z corresponding to the current loops has a quadrupole structure. The Hall current structure as a typical

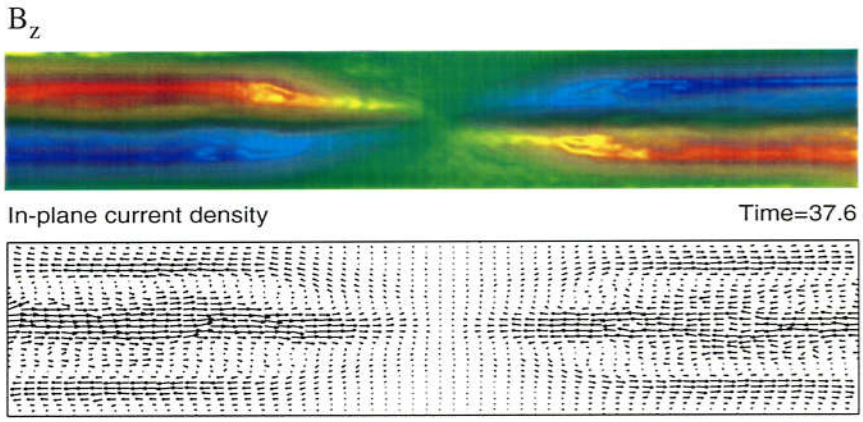

Figure 4.12: The Hall current system: out-of-plane magnetic field B_z (top panel) and in-plane current (bottom).

character of collisionless reconnection has been seen before in the particle and hybrid simulations of reconnection [37, 55, 61]. Recently, Nagai *et al.* [8] observed electrons flowing into the reconnection region, a part of the Hall current system, near the boundary region of the plasma sheet for substorm onsets.

4.3.4 Discontinuities

The discontinuities arise near the peak positions of B_z (see Fig. 4.4), which are often called the slow shock. In order to see these features of the discontinuity clearly, we plot the profiles of densities, x and z components of velocities of ion and electron flows along the vertical line $x = 261\lambda_{d0}$ ($\approx 0.68x_b$) in figure 4.13. The discontinuity causes the electron and ion flows to turn their directions toward the outflow, and both their densities and temperatures (see Fig. 4.7) to increase as well. The discontinuity width is of the electron scale, e.g., δ_e, from the profile of electron flow component u_{ex}. The discontinuities contain concentrated out-of-plane electric currents, as shown in Fig. 4.5. Since $\mathbf{j_e} \cdot \mathbf{E} > 0$, the entire discontinuities along with the the electron dissipation region acts as an energy convertor from magnetic energy into electron energy.

4.3.5 Current layer and reconnection rate

The electron dynamics and ion dynamics associated with different spatial scales display substantially different behaviors. However, the global dynamics is controlled by the massive ion dynamics because it determines the whole plasma density distribution. This result is in good agreement with the previous simulations [27, 30]. The electron dynamics fits in with the global evolution by adjusting itself. The Hall current system is a good example

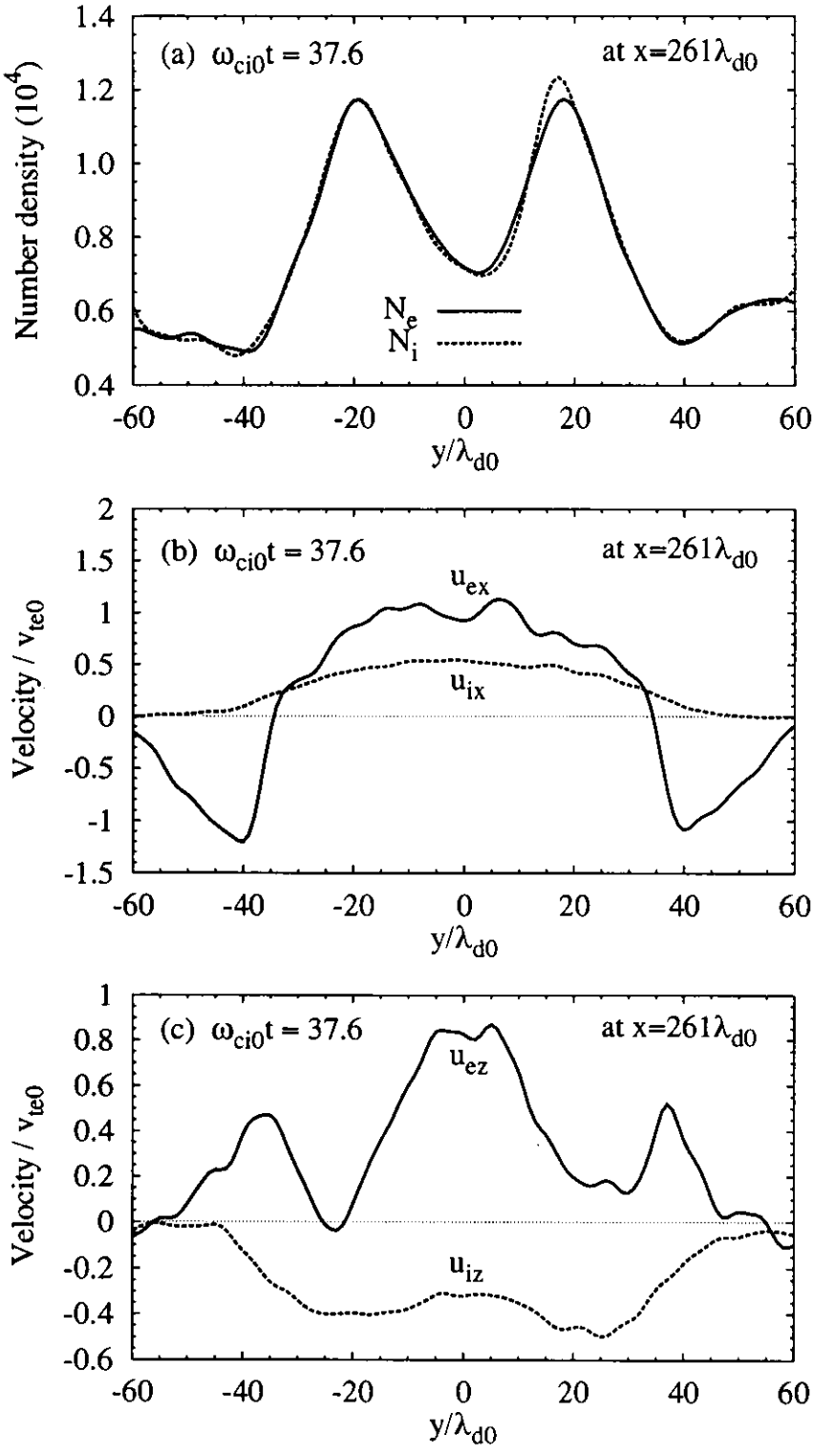

Figure 4.13: The profiles of (a) number densities N_e and N_i, (b) x components of velocities u_{ex} and u_{ix}, and (c) z components of velocities u_{ez} and u_{iz} of electron and ion flows along the vertical line $x = 261\lambda_{d0}$.

of the electron adjustment. In order to make up for the depletion of electron inflow flux supplied from the upstream boundary, the upstream electrons convergently flow toward the reconnection region which results in the Hall current.

A second example is the relation between electron inertia scale and orbit size (see Fig. 4.3), $l_{me} \sim \delta_e$, which seems to be universal because they have the same scale with $m_e^{1/2}$. Using Eq. (4.1), we have

$$B_x(\delta_e) \sim \sqrt{4\pi n_e T_e}. \tag{4.9}$$

That is, the magnetic field at the inflow edge of the electron dissipation region is independent of the electron mass, but dependent on n_e controlled by ions, noting that T_e is almost unchanged. Therefore, the reconnection rate, the electron inflow velocity $cE_0/B_x(\delta_e) \sim cE_0/\sqrt{4\pi n_e T_e}$, is dependent on the ion dynamics but not the electron dynamics.

Furthermore, the global dynamics dominated by the ion dynamics is also seen in the structure of the current layer. Fig. 4.8(b) shows that the electron flow velocity u_{ez} is much higher than the ion flow velocity u_{iz} in the z direction, which means that most of electric current is carried by the electrons. However, the width of current layer is almost the same as the width of plasma density in the whole evolution of reconnection, and is of the scale of ion orbit size rather than the electron scale in the steady phase (see Fig. 4.3). The reason comes from the following two facts. First, the electron current is formed in the ion dissipation region because of the action of the electrostatic field. Second, the profile of electron current is mainly controlled by the electron density characterized by the ion orbit scale l_{mi}. On the other hand, the length of the current layer is determined by the electron dynamics, which is about the length of the electron dissipation region [see Fig. 4.5(a)].

This argument is helpful to understand why the steady reconnection rate is controlled by the external driving electric field but independent of the internal processes such as electron dynamics and ion dynamics (see Fig. 4.2). That is, the global dynamical behavior of collisionless reconnection is determined by the ion dynamics which is controlled by the external driving electric field. This result is important to explain many realistic phenomena relevant to fast reconnection. Our result also supports the conclusion from the previous studies of collisionless reconnection in a driven system with periodic downstream boundaries [27] or in a closed system [30, 33, 34, 35, 36, 37]. They found that the reconnection rate is controlled by the ion dynamics and is essentially independent of the electron mass and thus mechanism by which the electron frozen-in condition is broken.

The realization of steady reconnection implies that the internal processes (electron dynamics and ion dynamics) can adjust themselves to accommodate the external driving condition. Otherwise, the magnetic reconnection evolves intermittently. In Chapter 5, we will investigate the mechanism of intermittent phenomena.

Chapter 5

Intermittent Behavior in Reconnection

It is shown in Table 3.1 that the intermittent phenomena can take place only in the cases of $x_d/x_b = 0.83$. We explore the mechanism of intermittent phenomena in the evolution of driven reconnection. In section 5.1 the characteristic features of intermittent phenomena are given based on Run 3. The control mechanism of island growth is described in section 5.2. The influence of driving field on the current layer structure are investigated in section 5.3. In section 5.4 the mechanism of intermittent phenomena is discussed.

5.1 Overview of intermittent behavior

Figure 5.1 plots the magnetic field configurations at ten different times for Run 3. A small magnetic island is created at $\omega_{ci0}t = 5.7$. This island grows with time while moving to the left. The system relaxed to a state without any island (see the fifth panel) after the island moves out through the left boundary. However, the evolution of magnetic field for Run 3 after $\omega_{ci0}t = 22.0$ is distinctly different from that for Run 1 (Fig. 4.1). One can see that there appears a magnetic island from the center near the original X point at $\omega_{ci0}t = 22.9$. It grows and moves to the right and then goes out of the system. When the island goes out, another island is produced near the center. In this way islands repeatedly arise one after another. The system cannot relax to a steady state, but behaves intermittently. This picture exhibits a typical character of tearing instability because of the frequent generation of magnetic islands. In the other words, the intermittent behavior is related to collisionless tearing instability.

Figure 5.2 shows the histories of (a) the reconnection electric field E_r and (b) current layer width d_{jz}, ion meandering orbit size l_{mi}, electron meandering orbit size l_{me} and electron skin depth δ_e at the main X point for Run 3. In the saturation phase, the reconnection electric field in the intermittent case oscillates around the value of the external

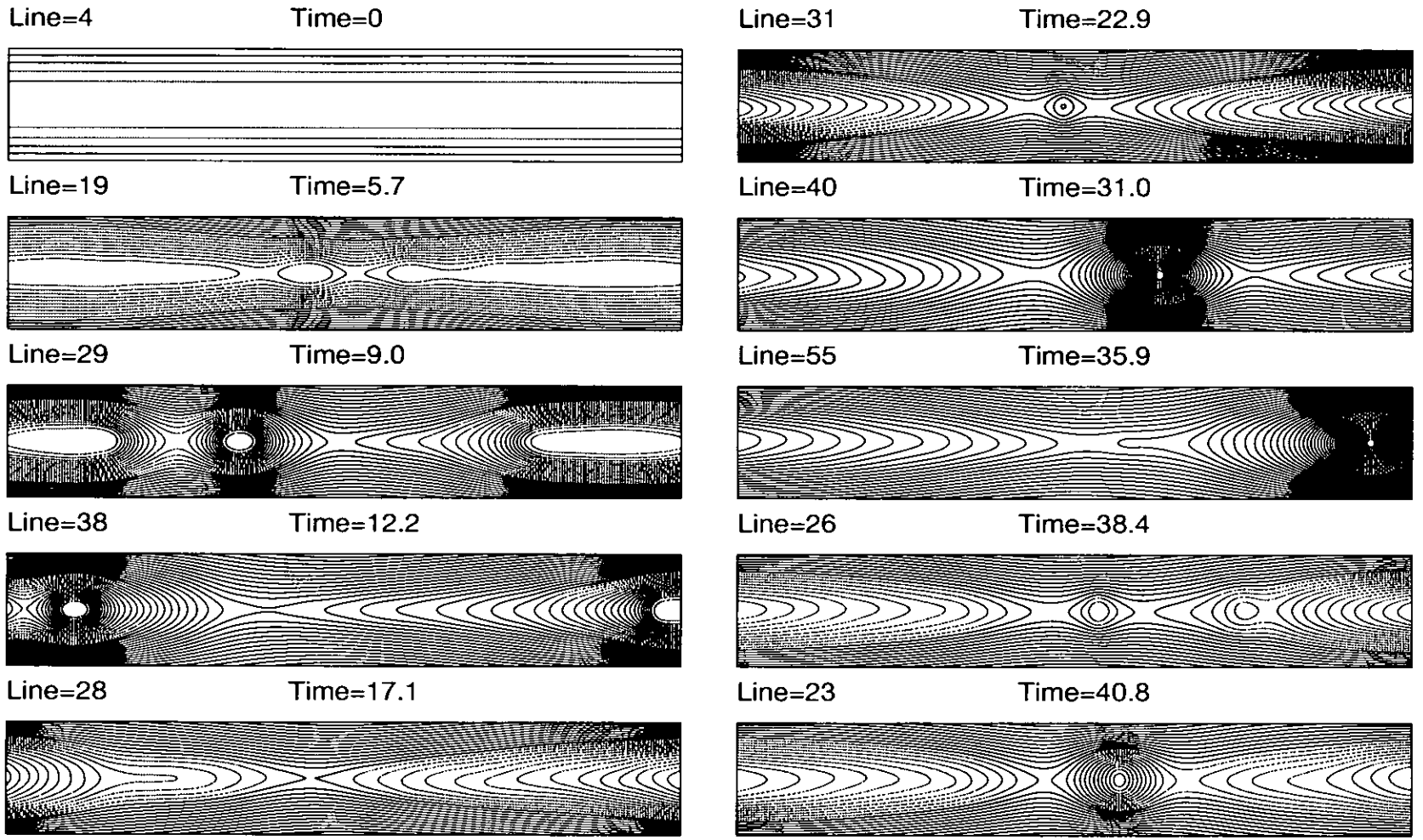

Figure 5.1: The temporal evolution of magnetic field configuration in the x-y plane for Run 3 where the time unit is ω_{ci0}^{-1}.

driving field E_0 with a larger amplitude compared with Run 1. Nevertheless, the reconnection rate is also determined mainly by the external driving electric field E_0. One can find that there is a correlation between the growth of islands and the behaviors of these quantities. When an island is produced at the central region (for example, at $\omega_{ci0}t = 22.0$, 36.7 and 52.8), $|E_r|$ is minimum. As the island grows, the width of current layer at the main X point decreases below l_{mi} and $|E_r|$ evolves toward a maximum. When the island is far away from the center, d_{jz} returns to l_{mi}.

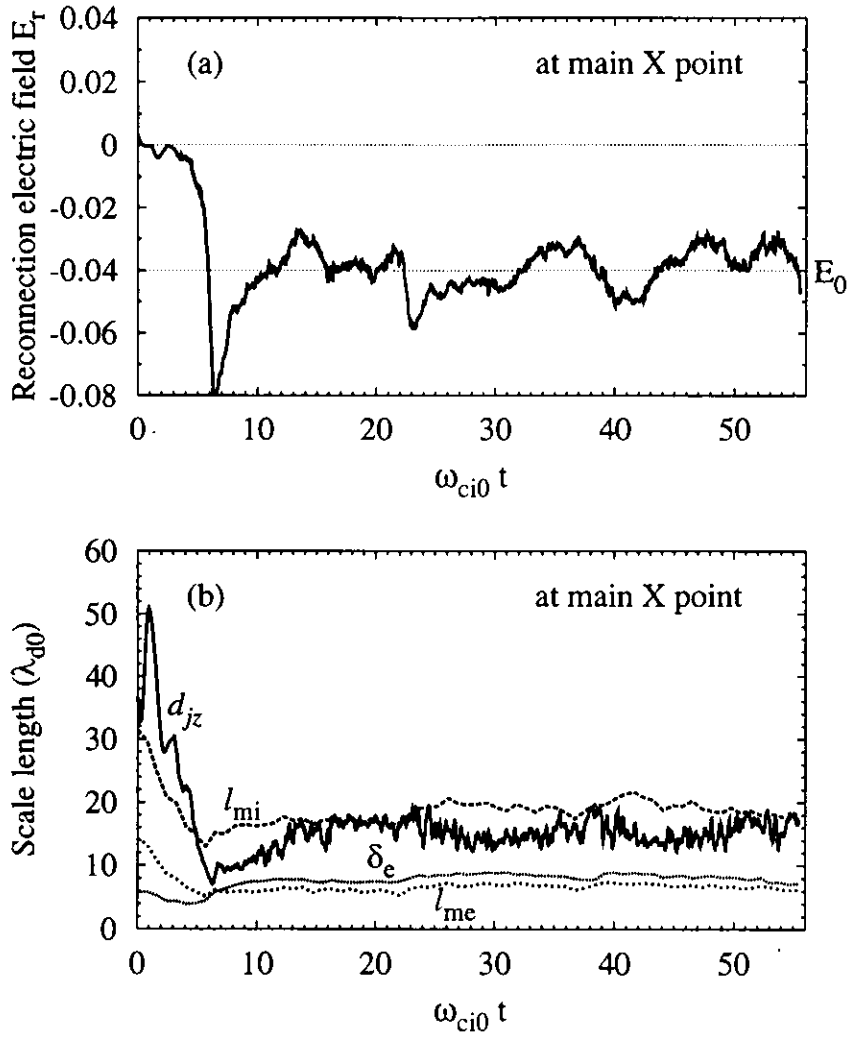

Figure 5.2: The time histories of (a) reconnection electric field E_r and (b) four spatial scales, d_{jz}, l_{mi} l_{me} and δ_e at the main X point for Run 3.

5.2 Control mechanism of island excitation

Let's examine which of electrons and ions are the dominant carrier of electric current leading to the growth of an island. Figure 5.3 shows the profiles of the total current density $-j_z$, the electron current $-j_{ez}$ and the ion current $-j_{iz}$ along the x axis at $\omega_{ci0}t = 39.2$ when the island is growing. The island is located at the peak position of the current density $-j_z$. It is clear from Fig. 5.3 that the electrons are the dominant carrier of the electric current. This result implies that electron dynamics is important for island growth. So we can conclude that the intermittent phenomena result from electron tearing instability not ion tearing instability.

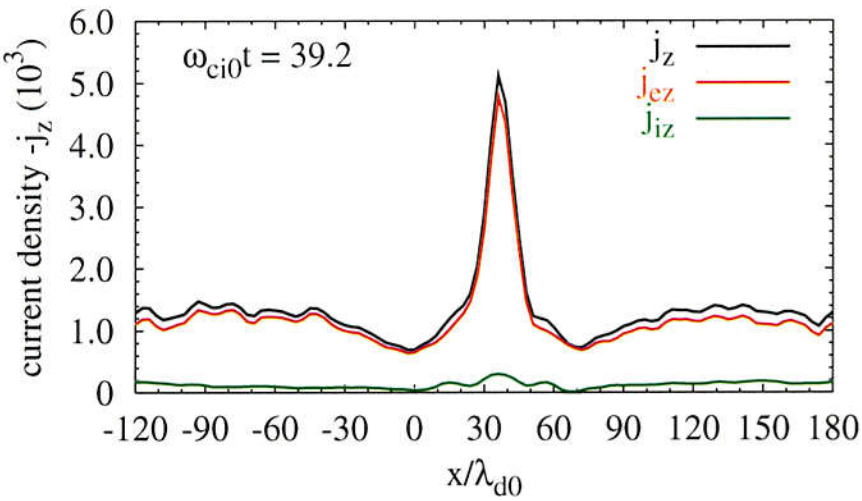

Figure 5.3: The profiles of the total current density $-j_z$, the electron current $-j_{ez}$ and the ion current $-j_{iz}$ along the x axis when the island is growing.

Let us clarify the mechanism leading to the excitation of an island by examining the spatial structure of the physical quantities for electrons when an island is formed and growing up. Figure 5.4 shows the spatial configurations of the magnetic field and color-coded contour maps of the current $-j_z$, the electron flow velocity u_{ez} and the electron number density at $\omega_{ci0}t = 37.6$ and 39.2 where the left panels correspond to the time just when the island is formed and the right panels to the time when island is growing. The electric current rises locally inside the island. Two islands are excited by the locally enhanced current density, but only the one near the center can grow up. Figure 5.4 reveals the following three facts. First, the island is formed when the current layer becomes narrower and longer compared with Run 1, which facilitates the tearing instability. Second, the island is originally triggered due to the perturbation of electron velocity u_{ez} (see the third panel on the left). Third, the island growth requires electric current increase in

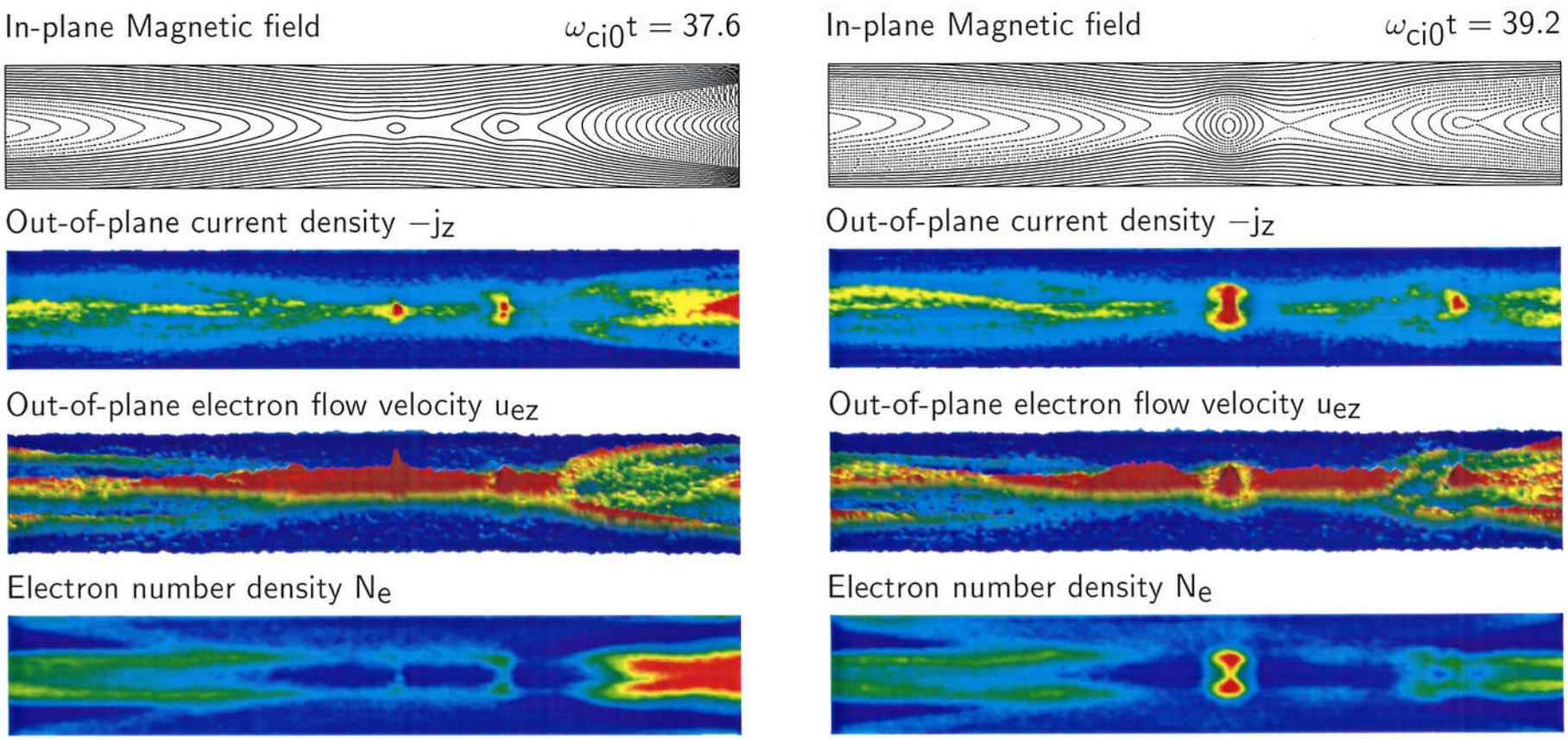

Figure 5.4: The spatial configurations of the magnetic field and perspective views of the current $-j_z$, the electron flow velocity u_{ez} and the electron number density at $\omega_{ci0}t = 37.6$ and 39.2 where the left panels corresponds to the time just when the island is formed and the right panels to the time when island is growing.

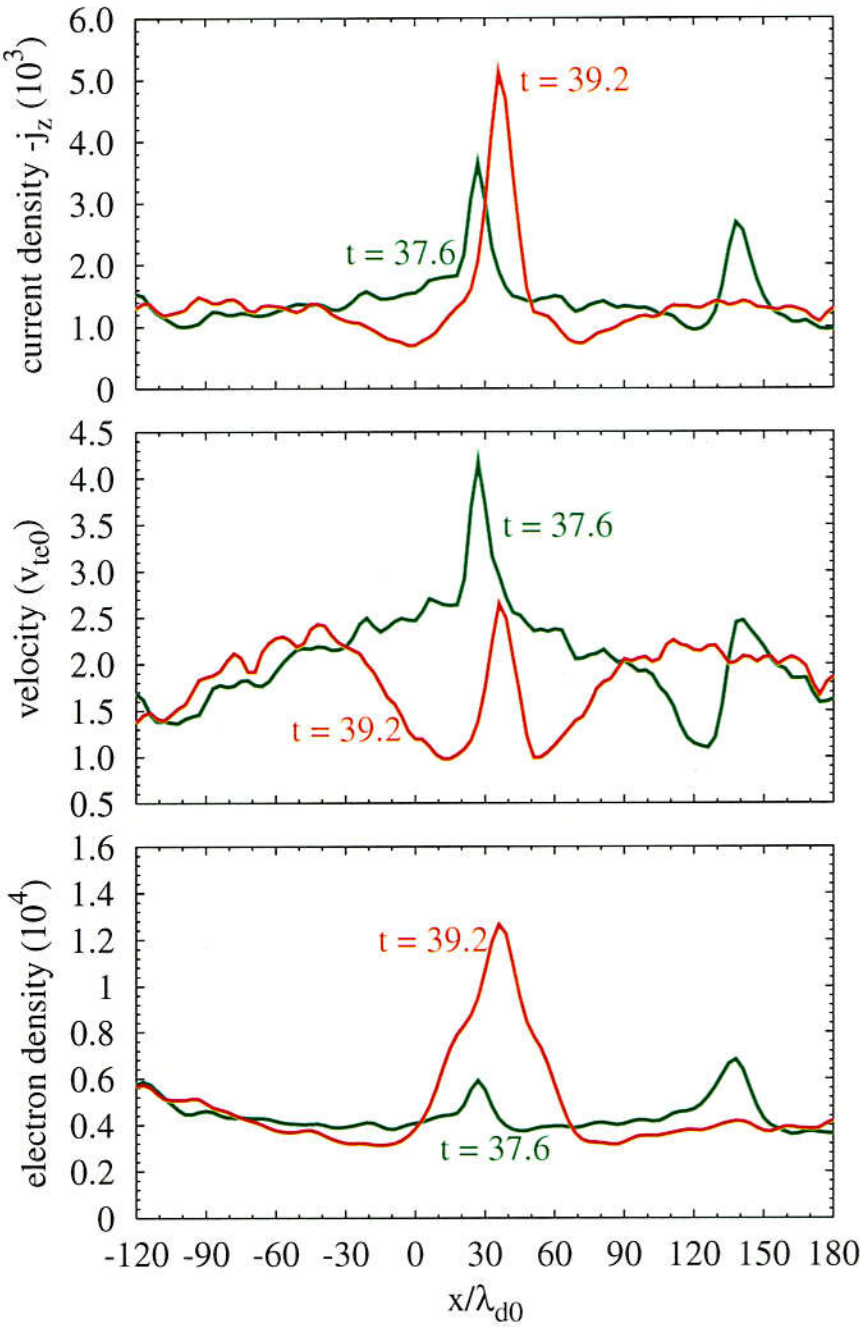

Figure 5.5: The profiles along the x axis of (a) the current density $-j_z$, (b) the electron velocity u_{ez} and (c) the electron density n_e corresponding to Fig. 5.4.

it. Comparing the quantities at two times, one can find that the current increase is due to the contribution of electron density rather than electron velocity. In order to see this point clearly the profiles of these quantities along the x-axis are plotted in Fig. 5.5. It can be seen that as time goes on the electron density increases while the electron velocity decreases at the center of the island. The density increase is caused by the electron trapping inside the island. Therefore, the electric current needed for the growth of the island is supplied by increasing the electron number density.

In summary, the intermittent behavior in the evolution of driven reconnection for $x_d/x_b = 0.83$ results from the excitation of collisionless tearing instability through which islands are frequently created. More precisely, the electron tearing mode is its cause because the electron current dominates over the ion current. A seed island is triggered due to the perturbation of electron velocity. The increase in the electric current supporting the growth of the island comes mainly from the increase in the electron density through the electron trapping in the island. In the next two sections we will explore the detailed mechanism that leads to the excitation of the electron tearing instability.

5.3 Influence of external driving field

In this section we consider why the behavior of driven reconnection is dependent on the nonuniformity scale x_d but independent of the driving field strength E_0. We examine the influence of the driving parameters on the spatial structure of the current layer based on the simulation resluts in the steady cases. The dependences of the electron number density (top), the electron out-of-plane flow velocity (middle), and the half-width of the current profile (bottom) at the X point on the scale x_d are plotted in Figure 5.6. It can be seen that, as x_d increases, the electron density increases and the current layer becomes narrow, while the electron flow velocity remains almost constant. This phenomenon can be explained as follows. As x_d increases, the curvature of magnetic field lines and the divergency of the corresponding plasma inflow near the upstream boundary decrease. Consequently, the particle number entering the reconnection region increases and the current layer is more strongly compressed with increasing x_d, which leads to the density increase. In other words, the parameter x_d controls the density profile of the current layer through the ion dynamics.

Figure 5.7 shows the dependences of the electron number density, the electron out-of-plane flow velocity, and the half-width of the current profile on the driving field strength E_0. As E_0 increases, both electron number density and electron out-of-plane flow velocity increase and the current layer becomes narrow. The density increase is deeply related to the fact that the input plasma flow flux increases in proportion to E_0. The electron velocity increase is due to the electron acceleration by the electric field E_z .

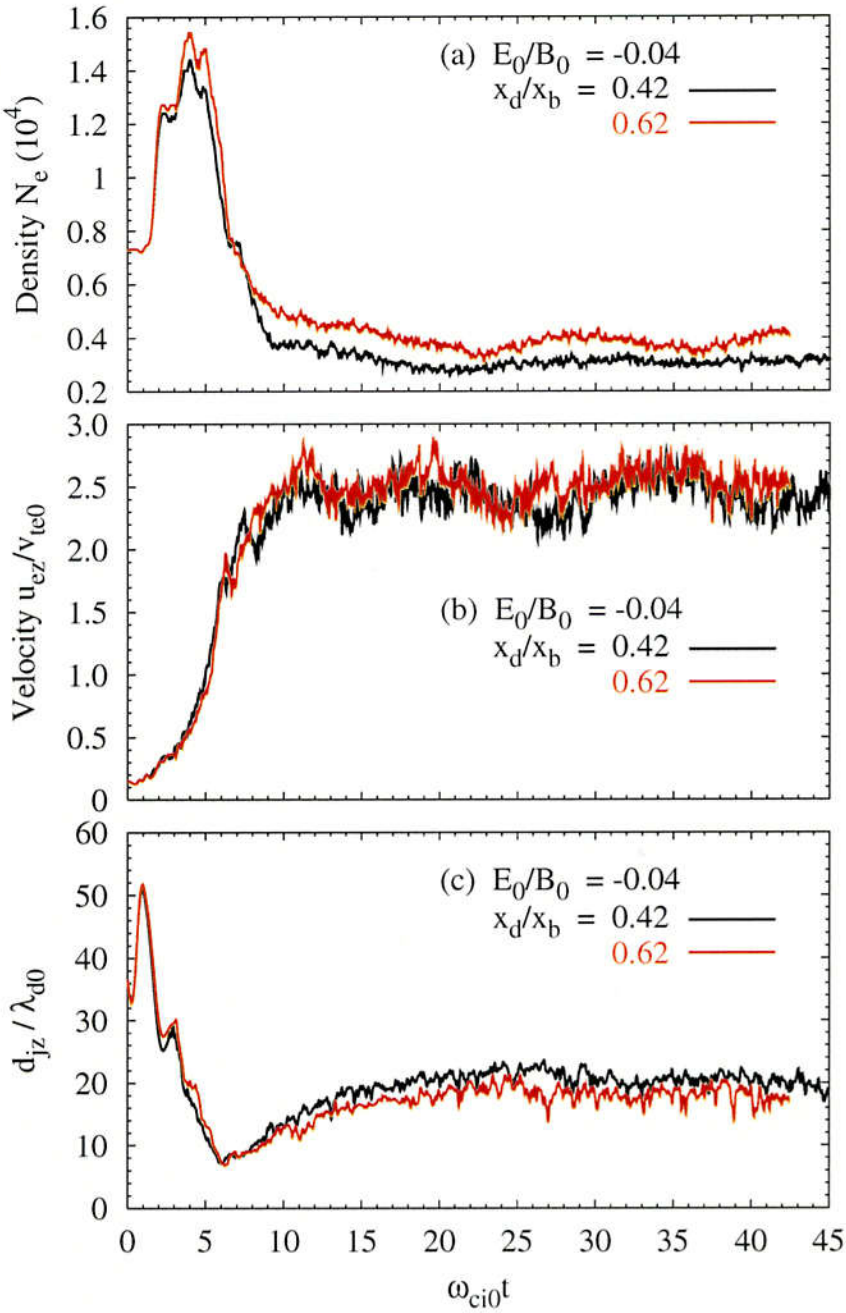

Figure 5.6: The histories of (a) electron number density N_e, (b) electron flow velocity u_{ez} and (c) half-width of current layer at the X point for Runs 1 and 2.

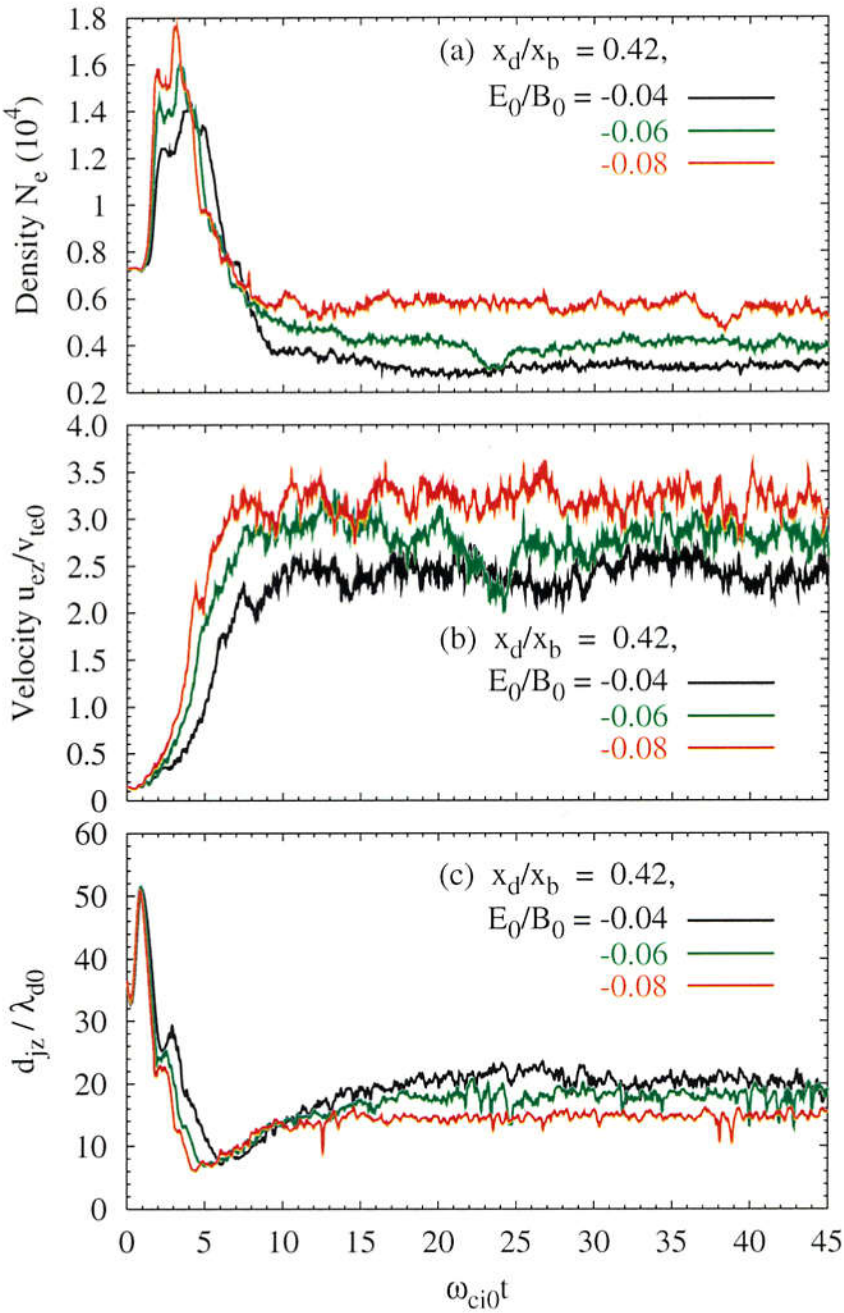

Figure 5.7: The same figure as Fig. 5.6 for Runs 1, 4 and 7.

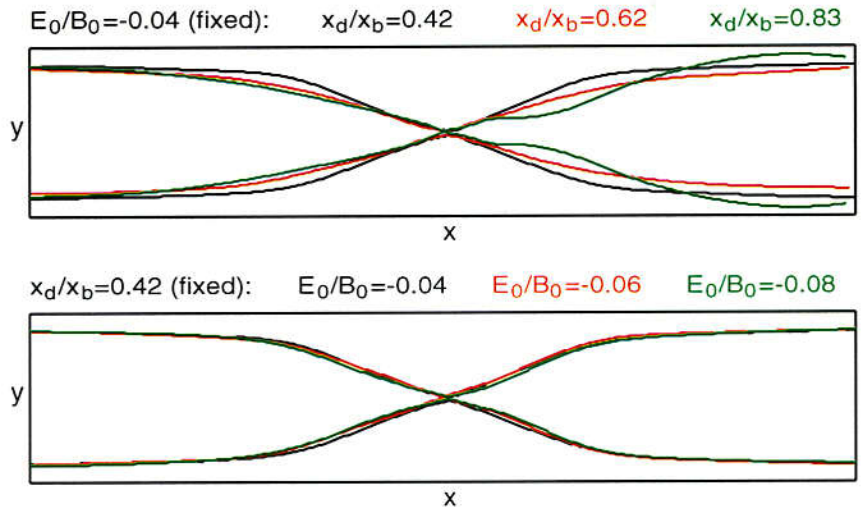

Figure 5.8: Comparison between the separatrix shapes for different x_d (top panel) and for different E_0 (bottom panel).

Let us examine the global structure of the current layer and the corresponding magnetic field configuration. Figure 5.8 plots the structures of the magnetic separatrix for different x_d (top) and for different E_0 (bottom). For comparison, we plot, in the top panel, the separatrices at $\omega_{ci0}t = 35.9$ just before an island is formed in the intermittent case (Run 3). Figure 5.8 demonstrates that the angle θ between separatrices in the downstream region reduces distinctively as x_d increases, but is insensitive to E_0. These results mean that the shape of current layer is also changed, which is discussed as follows.

If we expand the magnetic field near the X point (the origin) into a Taylor series and keep only the first-order, then the field components are

$$B_x = B_{x0}\frac{y}{d_{jz}} \qquad |y| \leq d_{jz}, \tag{5.1}$$

$$B_y = B_{y0}\frac{x}{L_{jz}} \qquad |x| \leq L_{jz}, \tag{5.2}$$

where d_{jz} and L_{jz} are the half width and half length of the current layer. The corresponding vector potential is

$$A_z = \frac{B_{x0}}{2d_{jz}}(y^2 - a^2x^2) + A_0(t), \tag{5.3}$$

where $\partial_t A_0 = cE_0$ and $a^2 = d_{jz}B_{y0}/L_{jz}B_{x0}$. Using the relation, $d_{jz}B_{x0} = L_{jz}B_{y0}$, the parameter a can be written as $a = d_{jz}/L_{jz}$ representing the shape of current layer, or $a = B_{y0}/B_{x0}$ being the ratio of reconnected field to unreconnected field. The field lines are described by the condition $A_z(x(t), y(t), t) = const$, moving with the velocity $\mathbf{E} \times \mathbf{B}/B^2$

except the separatrices. The separatrices are the field lines through the X point (located at the origin of coordinates)

$$y = \pm ax \tag{5.4}$$

so that the separatrix angle in the downstream region is expressed as

$$\theta = 2\tan^{-1}a. \tag{5.5}$$

The angle θ or value a $(= \tan(\theta/2))$ is related to the current density

$$j_z = \frac{c}{4\pi}(\nabla \times \mathbf{B})_z = -\frac{c}{4\pi}\left(\frac{B_{x0}}{d_{jz}} - \frac{B_{y0}}{L_{jz}}\right) = -\frac{cB_{x0}}{4\pi d_{jz}}(1 - a^2). \tag{5.6}$$

In our cases, the width of current layer is approximately equal to the ion Larmor radius, i.e., $d_{jz} \approx l_{mi} = \rho_i$, and thus $B_{x0} \sim 1/d_{jz}$. Although increases both in x_d and in E_0 lead to narrowing of the current layer and increase in the current density, the resulting change in the shape of current layer is quite different for the two parameters. According to the above relations, as x_d increases, the separatrix angle θ decreases, and thus the aspect ratio of the current layer L_{jz}/d_{jz} $(= 1/a)$ increases, that is to say, the shape of current layer becomes narrow and flat. On the contrary, when E_0 increases, the current layer is only similarly compressed. Thus, the aspect ratio of current layer, or its shape, remains unchanged. The dependence of the current layer shape and so the magnetic field configuration on the external driving field is the key to understand the intermittent behavior of reconnection because large aspect ratio of the current layer facilitates the excitation of electron tearing instability.

The profiles of the reconnected magnetic fields along the x-axis $(y = 0)$ for different values of x_d are plotted in Fig. 5.9. The derivative $\partial_x B_y$ $(\approx B_{y0}/L_{jz})$ is almost independent of x_d near the X point. That is, B_{y0} and L_{jz} are insensitive to x_d due to the relation $L_{jz}B_{y0} = d_{jz}B_{x0}$. This result is consistent with the fact that the electron out-of-plane flow velocity u_{ez} at the X point is independent of x_d as shown in Fig. 5.6(b). These results imply that the electron outflow in the dissipation region is not affected by x_d because $u_{ez}B_{y0}/c$ force is independent of x_d. Thus, as x_d increases, the increasing gradient of the unreconnected field B_x is the main reason for the decrease in separatrix angle. The current density j_z is dominated by term B_{x0}/d_{jz} from Eq. (5.6) because of the relation $B_{x0}/d_{jz} \gg B_{y0}/L_{jz}$. As a result, the electron density increases with x_d [see Fig. 5.6(a)] according to the scaling as

$$n_e \propto j_z \sim \frac{B_{x0}}{d_{jz}} \propto B_{x0}^2, \tag{5.7}$$

where $d_{jz} \approx l_{mi} \approx \rho_i(d_{jz})$ is used. Relation (5.7) is actually the same as Eq. (4.9), i.e., $\delta_e \approx l_{me}$, discussed in the previous chapter.

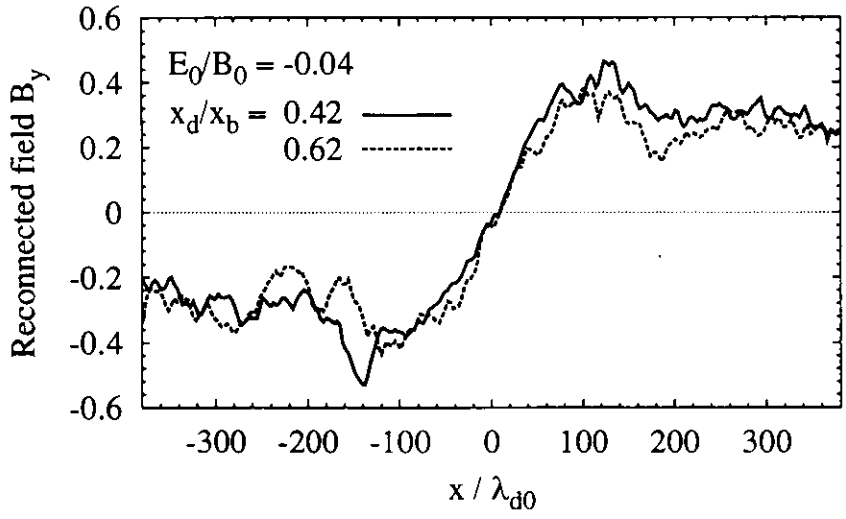

Figure 5.9: The profiles of the reconnected magnetic fields B_y along the x axis for different x_d.

5.4 Electron tearing instability

In this section we discuss the excitation mechanism of the electron tearing instability which causes an intermittent behavior of reconnection.

A magnetic island often arises near the original X point where the magnetic field vanishes and the current density is locally maximum. As long as there is a perturbation, an island structure is easily formed near the X point. However, not all the perturbed islands can grow up. Because the growth of an island requires some mechanism to increase electric current in it, only the islands which satisfy some condition can grow up. Figure 5.4 indicates that the current increase results from the density increase due to the electron trapping inside the island. Let us estimate the condition for the electron trapping inside an island from the standpoint of force balance. The electron trapping is realized when the magnetic tension (pinching force) overcomes the pressure gradient force in the x direction

$$-\frac{en_e u_{ez}}{c} B_y - \frac{\partial P_e}{\partial x} > 0. \tag{5.8}$$

Using $j_z \approx en_e u_{ez}$ and Ampere's law, we rewrite the above relation as

$$\frac{1}{4\pi} B_y \left(\frac{\partial B_x}{\partial y} - \frac{\partial B_y}{\partial x} \right) > T_e \frac{\partial n_e}{\partial x}. \tag{5.9}$$

Defining the island size w as the distance of the B_y peak from the O point along the x axis ($y = 0$), the relation (5.9) reduces to

$$w > l_{me}^y \left(\frac{l_{me}^x}{\delta_e} \right)^2, \tag{5.10}$$

where l_{me}^x and l_{me}^y are respectively the electron meandering orbit sizes associated with B_x and B_y. (Note superscript corresponding to the component of magnetic field.) If we use the simulation result that l_{me}^x is slight less than δ_e, the necessary condition for island growth is that the size of a perturbed island w should be larger than the electron meandering orbit size l_{me}^y in the x direction. This is the condition for a long-wave instability. According to this criterion one can understand easily why collisionless reconnection becomes intermittent when x_d/x_b increases to 0.83.

The simulation results shown in Figs. 5.4 and 5.5 indicate that the perturbation of the electron out-of-plane flow velocity u_{ez} gives rise to a local enhancement in the electric current profile and triggers a seed island near the original X point. The electron velocity perturbation results from acceleration in the out-of-plane direction by the reconnection electric field around the X point where the x component of flow velocity is nearly equal to zero. The width of the acceleration region is controlled by the electron meandering orbit amplitude l_{me} ($\sim B_{x0}^{-1}$). Supposing that the perturbation of the electron out-of-plane flow velocity δu_{ez} is located at the origin of coordinates $[(x, y) = (0, 0)]$, the corresponding perturbed magnetic field amplitude on the x-axis ($y = 0$) is estimated using the integral form of Ampere's law as

$$\delta B_y(x) \sim -\frac{(4\pi/c)en_e\delta u_{ez}l_{me}d_x}{\pi(l_{me}+d_x)} \propto -\frac{l_{me}d_x}{l_{me}+d_x}n_e\delta u_{ez} \propto -B_{x0}^{1\sim 2}\delta u_{ez}, \tag{5.11}$$

where the relation (5.7) has been used and d_x is the perturbation size in y direction. Here, d_x is independent of x_d because B_y is unchanged with x_d. It is seen that as x_d increases B_{x0} increases and thus the perturbed field δB_y increases. In other words, the perturbed island size which is determined from the superposed profile of $B_{y0}+\delta B_y$ increases with x_d. When the condition $w > l_{me}^y$ is satisfied, the perturbed island can grow up. That is, in the big x_d case (e.g., $x_d/x_b = 0.83$) the electron tearing mode becomes unstable and grows up. This is why the intermittent phenomena take place in the cases of $x_d/x_b = 0.83$.

On the other hand, because the global shapes of magnetic separatrices and so the current layer remain almost unchanged when the strength E_0 changes, the tearing instability is insensitive to the change in the strength E_0. It is concluded that in a large x_d case collisionless reconnection reveals an intermittent behavior through the frequent generation of magnetic islands because the current layer becomes unstable against the electron tearing instability.

The intermittent phenomena is energetically favored. In a driven magnetic reconnection, the plasma inflow carries a large amount of magnetic energy into the system through the upstream boundaries and flows toward the dissipation region. Most of magnetic energy is converted into plasma energy by means of magnetic reconnection process. The unconverted magnetic energy is carried out of system by plasma outflow. The reconnection rate is dominantly controlled by the driving electric field E_0. This is the physical

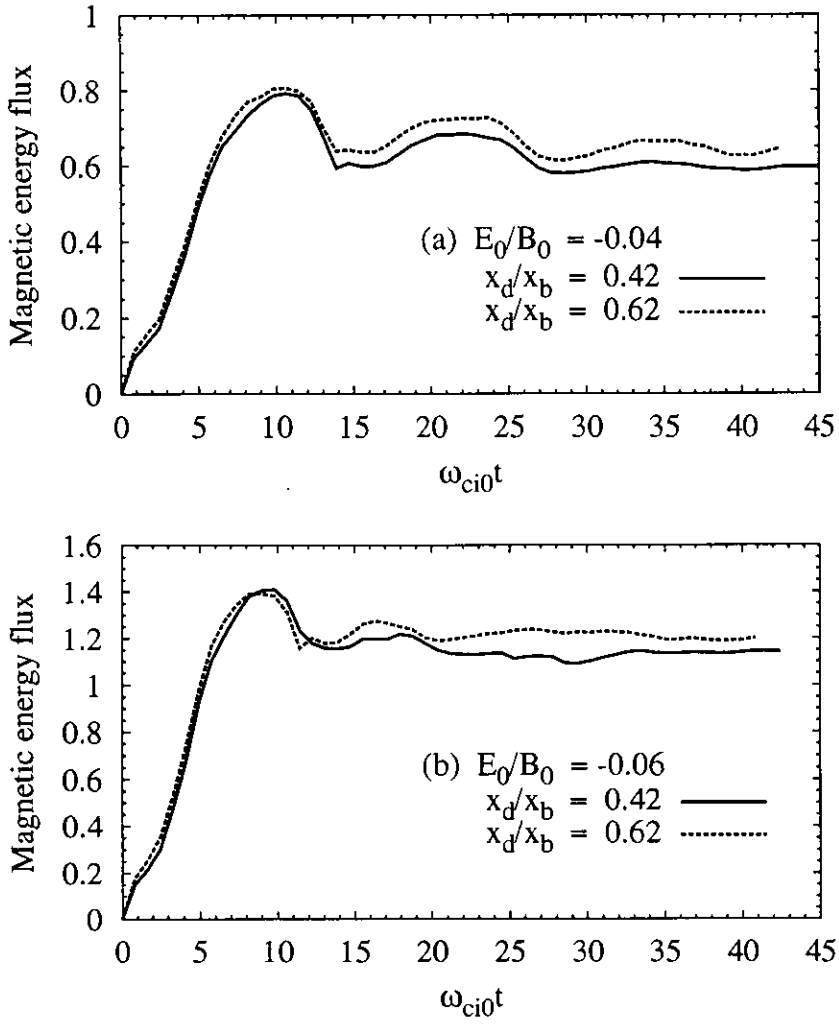

Figure 5.10: The histories of input magnetic energy flux for different x_d with (a) $E_0/B_0 = -0.04$ and (b) $E_0/B_0 = -0.06$.

picture of the steady reconnection which works in the small x_d case. The nonuniform scale x_d controls the patterns of input magnetic flux and input plasma inflow. The curvature of magnetic field lines and the divergency of the corresponding plasma inflow near the upstream boundary decrease as x_d increases. Figure 5.10 shows the change of the input magnetic energy flux for two different values of x_d in the steady cases. The input magnetic energy flux increases with x_d. As x_d increases the separatrix angle decreases, which implies that the energy conversion (or magnetic energy loss) efficiency , $(B_{x0}^2 - B_{y0}^2)/B_{x0}^2 = 1 - a^2$, increases by narrowing the current layer. When x_d/x_b increases up to some critical value (for instance, 0.83), the reconnection with single X point structure can not convert the enough magnetic energy into plasma kinetic energy. Consequently, the density accumulation occurs near the X point and thus a magnetic island is formed. It is evident that the formation of the island is an effective way to relax the energy release and store up energy.

Chapter 6

Conclusion and Discussion

We have presented first results of particle simulation of collisionless driven reconnection in an open system. In order to study the long time scale evolution of collisionless driven reconnection, we have developed a new simulation model for an open system. In this model, a free physical condition is used at the downstream boundary, across which particles can freely go in and out. At the upstream boundary the driving condition can be uniquely determined by an out-of-plane electric field which is described by two key parameters, the strength E_0 and the early non-uniformity scale x_d. The strength E_0 represents the input magnetic flux rate and the scale x_d controls the patterns of input magnetic flux and thus the input plasma inflow.

In order to study dependence of the long-time scale behavior of collisionless reconnection on the external driving condition, we have carried out nine simulation runs with various sets of E_0 and x_d. The simulation parameters and one of important results of these runs are listed in Table 3.1. The simulations show that the evolution of collisionless driven reconnection depends strongly on the external driving electric field. The strength E_0 controls the reconnection rate, while the scale x_d controls the current layer shape and thus the magnetic field configuration. It is found that there are two regimes in the long time scale behavior of collisionless driven reconnection which is mainly controlled by the scale x_d in our simulation parameter range, i.e., steady regime and intermittent regime. In a small x_d case the system evolves toward the steady regime in which steady reconnection is realized and thus the global field topology remains unchanged. On the other hands, in a large x_d case the system evolves into the intermittent regime in which magnetic islands are frequently formed near the center of the current sheet.

Steady reconnection

We have investigated the physical features of the steady reconnection. The evolution of collisionless reconnection consists of two temporal phases, growing phase and saturation

phase. The behavior of reconnection in the growing phase coincides with that of the previous periodic simulation [27, 28]. During the saturation phase the system gradually tends to a steady state. The main results of steady reconnection are summarized as follows.

(1) The steady reconnection rate is mainly controlled by the strength of the driving electric field E_0.

(2) The dissipation region has two-scales structure corresponding to both the electron dynamics and the ion dynamics. The electron motion decouples from the magnetic field in the electron dissipation region with the half-width of δ_e. The ions become unmagnetized due to the ion inertia effect in the ion dissipation region which is $2\delta_i$ wide.

(3) Despite the ion inertia effect responsible for breaking down the ion frozen-in constraint, the ion meandering motion plays an important role in ion dynamics which characterizes the spatial structures of plasma density, ion flow velocity and ion temperature with the scale of l_{mi}.

(4) The decoupling of ion motion and electron motion (the Hall term) in the ion dissipation region, in particular in the scale of ion meandering motion, produces an electrostatic field E_y in the inflow direction due to small charge separation (the finite Larmor radius effect). This electrostatic field is a key to coordinate the motions of electrons and ions. The field E_y leads to ion heating by reinforcing ion bouncing motion. As a result, the distribution function of ion inflow velocity consists of two counter-streaming components near the center of the bounce motion. The nonclassical ion heating in the reconnection layer has been found in the recent MRX experiment [48, 49] and in the TS-3 experiment [50]. In contrast with ions, the electrons are made to drift in the out-of-plane direction under the action of E_y before entering the electron dissipation region, which leads electrons to accelerate above their thermal velocity. In the electron dissipation region, electrons are hardly heated because E_y weakens the electron bouncing motion. As a result, the electron inertia effect dominates over its thermal effect in breakdown of the frozen-in constraint.

(5) As a result of the action of the electrostatic field, the current layer is formed in the ion dissipation region. Although the current is predominantly carried by electrons, the current layer has the half-width of the ion scale l_{mi} because of the influence of the density profile which is exclusively controlled by the massive ion motion. Although this result differs from those from the simulations of non-driven reconnection in a closed system, it is in good agreement with the recent measurement of MRX experiment [48].

(6) The electron heating occurs when the electron motion becomes magnetized again in the downstream.

(7) The different dynamic behaviors between electrons and ions brings about the Hall current loops which produces a quadrupole structure in the out-of-plane magnetic field.

This Hall current system ensures that electrons in upstream region can flow convergently toward the reconnection region along the magnetic field lines.

(8) Thus the above features lead us to a conclusion that the global dynamical process of steady magnetic reconnection is dominantly controlled by ion dynamics. This conclusion is consistent with the result from the previous studies [27, 30, 31, 33, 34, 35, 36, 37] that the reconnection rate is controlled by the ion dynamics.

It is worthy of notice that the present simulation has been carried out in the case of a relatively small mass ratio ($m_i/m_e = 25$). Let us consider what happens by increasing the mass ratio toward the real value. The size of electron dissipation region becomes much smaller than the ion dissipation size because it scales as $m_e^{1/2}$. According to the present conclusion, however, we may expect that the global behavior of collisionless driven reconnection is controlled by ion dynamics and so the electron dynamics accommodates itself to the surroundings, i.e., ion dynamics. This problem should be clarified in the future work.

Intermittent behavior of reconnection

As the non-uniformity scale x_d increases, the evolution of collisionless reconnection becomes intermittent. The transition from the steady to the intermittent regime is independent of the driving field strength E_0. The dynamics in the intermittent regime of collisionless driven reconnection has been studied. The main results are summarized as follows.

(1) The intermittent behavior is characterized by the frequent formation of magnetic islands near the original X points as a result of the excitation of collisionless tearing instability.

(2) Since the electron current dominates over the ion current in the current layer, the instability is excited by electron tearing mode but not by ion tearing mode. Island formation is triggered by perturbation in electron velocity. The electric current supporting the growth of an island comes mainly from the increase in the electron density through electron trapping in the island.

(3) The effect of the driving parameters E_0 and x_d on the current layer structure and the magnetic field configuration in the regime of steady reconnection has been examined. As E_0 increases, the current layer is similarly compressed, and thus the corresponding magnetic field configuration is almost unchanged. On the contrary, as x_d increases, the current layer becomes narrow and flat in shape. That is to say, the aspect ratio of current layer increases, and so the angle between the separatrices decreases. The electron density in the current layer increases with x_d.

(4) Excitation of tearing instability requires two conditions, i.e., a) formation of a seed

island and b) its growth. These conditions depend on the shape of current layer and the corresponding magnetic field configuration. The seed island is readily formed near the original X point due to the perturbation of electron velocity. The perturbed island size increases with x_d. The island growth requires the increase in the electron current which is mainly supplied by the increase in the electron density. Only the seed island with the spatial size larger than the electron meandering size can grow up by increasing the electric current through the electron trapping in it. Thus, in a large x_d case the system evolves into the intermittent regime in which magnetic islands is frequently created because of electron tearing instability.

(5) On the other hand, increase in E_0 dose not effectively change the magnetic field configuration. Thus the behavior of reconnection is insensitive to E_0.

The intermittent reconnection regime is regarded as one of energy relaxation processes. The input magnetic energy rate increases with the nonuniform driving scale x_d (see Fig. 5.10). Reconnection raises its energy conversion efficiency by flattening current layer under the limit of a fixed reconnection rate E_0. When the internal processes can not meet the external driving condition, e.g., in the case of $x_d/x_b = 0.83$, the magnetic island arises as an effective energy restoring way to relax energy release.

Here let us point out the difference between the conventional tearing instability and that in the intermittent regime in the present simulation. The conventional tearing instability is studied in a static case without any global plasma flow and its growth rate much smaller than an MHD rate. On the other hand, the intermittent behavior appears in a dynamical open system with a large plasma inflow and the island formation takes place in an MHD time scale. The difference in the growth time can be explained as follows. Reconnection field consists of fluctuating component and steady component which is equal to the external driving field. The island growth is determined by total amount of magnetic flux supplied into the island through reconnection at two X points on both sides. The external driving field used in the present paper is strong enough to carry the magnetic flux into the island through the X points in an MHD time scale. This is the reason why the island growth takes place in an MHD time scale. In other words the dynamical behavior of collisionless reconnection in a driven system is essentially controlled by the dynamics in an external region.

Appendix A

Boundary Conditions for the Maxwell Equations

We here discuss the problem of closing the Maxwell equations through the boundary conditions in 2D space.

In 2D space the fields may be divided into transverse electric (TE) and transverse magnetic (TM) sets. All spatial variation, or wave vector $\mathbf{k}$, is in the x-y plane. The TM fields, with $\mathbf{k} \cdot \mathbf{B} = 0$, have components E_x, E_y, B_z. The TE fields, $\mathbf{k} \cdot \mathbf{E} = 0$, have components B_x, B_y, E_z. The corresponding components of Maxwell equations can be rewritten as follows

TE set:

$$\frac{1}{c}\frac{\partial B_x}{\partial t} = -\frac{\partial E_z}{\partial y}, \tag{A.1}$$

$$\frac{1}{c}\frac{\partial B_y}{\partial t} = \frac{\partial E_z}{\partial x}, \tag{A.2}$$

$$\frac{1}{c}\frac{\partial E_z}{\partial t} = \left(\frac{\partial B_y}{\partial x} - \frac{\partial B_x}{\partial y}\right) - \frac{4\pi}{c} j_z, \tag{A.3}$$

TM set:

$$\frac{1}{c}\frac{\partial E_x}{\partial t} = \frac{\partial B_z}{\partial y} - \frac{4\pi}{c} j_x, \tag{A.4}$$

$$\frac{1}{c}\frac{\partial E_y}{\partial t} = -\frac{\partial B_z}{\partial x} - \frac{4\pi}{c} j_y, \tag{A.5}$$

$$\frac{1}{c}\frac{\partial B_z}{\partial t} = -\left(\frac{\partial E_y}{\partial x} - \frac{\partial E_x}{\partial y}\right). \tag{A.6}$$

It is seen that these sets are uncoupled with each other. Thus, we can consider the boundary condition for each set, respectively. In the following, we analyze the requirement for the boundary conditions under the assumption that the current density is known.

Case 1: Taking derivative of (A.6) with respect to t and using (A.4)-(A.5) we obtain

$$\frac{1}{c^2}\frac{\partial^2 B_z}{\partial t^2} - \frac{\partial^2 B_z}{\partial x^2} - \frac{\partial^2 B_z}{\partial y^2} = \frac{4\pi}{c}\left(\frac{\partial j_y}{\partial x} - \frac{\partial j_x}{\partial y}\right), \tag{A.7}$$

which is a wave equation. An extra condition on B_z at the 2D closed boundary is required for determining system evolution. That is, if B_z or its normal derivative dB_z/dl at the boundary is known, B_z is completely determined from Eq. (A.7). Then E_x and E_y are solved from (A.4)-(A.5), respectively. The similar discussion gives the boundary condition on E_z or dE_z/dl for the TE set. Therefore, the boundary conditions for whole fields require to know

$$\begin{cases} B_z, \quad \text{or} \quad \frac{dB_z}{dl}, & \text{for TM set.} \\ E_z, \quad \text{or} \quad \frac{dE_z}{dl}, & \text{for TE set,} \end{cases} \tag{A.8}$$

Case 2: In the same way, we can get, instead of B_z, the equations on E_x and E_y

$$\frac{1}{c^2}\frac{\partial^2 E_x}{\partial t^2} - \frac{\partial^2 E_x}{\partial y^2} = -\frac{\partial^2 E_y}{\partial x \partial y} - \frac{4\pi}{c}\frac{\partial j_x}{\partial t}, \tag{A.9}$$

$$\frac{1}{c^2}\frac{\partial^2 E_y}{\partial t^2} - \frac{\partial^2 E_y}{\partial x^2} = -\frac{\partial^2 E_x}{\partial x \partial y} - \frac{4\pi}{c}\frac{\partial j_y}{\partial t}. \tag{A.10}$$

The boundary condition is required by TM set as

$$\begin{cases} E_y, \quad \text{or} \quad \frac{\partial E_y}{\partial x}, & \text{at x-boundary,} \\ E_x, \quad \text{or} \quad \frac{\partial E_x}{\partial y}, & \text{at y-boundary.} \end{cases} \tag{A.11}$$

Similarly, TE set requires

$$\begin{cases} B_y, \quad \text{or} \quad \frac{\partial B_y}{\partial x}, & \text{at x-boundary,} \\ B_x, \quad \text{or} \quad \frac{\partial B_x}{\partial y}, & \text{at y-boundary.} \end{cases} \tag{A.12}$$

To sum up, each set needs only one boundary condition which is given by either (A.8) or (A.11)-(A.12).

Acknowledgments

I wish to express my gratitude to Professor Ritoku Horiuchi, my supervisor, for his patient and elaborate guidance and continuous encouragement which benifit me a lot throughout my graduate study and will certainly influence me in my future research.

I would like very much to thank Professor Tetsya Sato for providing me the opportunity to study plasma physics in Japan and bring me into the new field that I had not known but the term of reconnection before.

I am greatly indebted to Dr. Yukihiro Tomita for his kind help and support in my research and life in Japan.

Thanks are due to all members of Theory and Computer Simulation Center of National Institute for Fusion Science for their valuable advices and supports.

I would like to thank Ms. S. Urushihara for her all help.

Thank all the Japanese friends who helped me.

Numerical computations in this study is performed on the NIFS MISSION System (Grand Man-Machine Interactive System for Simulation).

Financial support by Society for Fusion Science is also acknowledged.

My appreciation is extended to Professor Xian-tu He, Professor Tieqiang Chang, Professor Weiyan Zhang and Professor Shao-ping Zhu of the Institute of Applied Physics and Computational Mathematics for their constant encouragement and support to me and for their help to my family in Beijing.

Special thanks go to my wife, Liang Chen, for her constant mental support, encouragement and endurance through my graduate life in which she has been bringing up my daughter on her own in Beijing. My deep sorry goes to my daughter, Yue Pei, for my absence during the important period of her growing up.

Bibliography

[1] K. Shibata, Adv. Space Res., 17, 9 (1995).

[2] E. R. Priest, Magnetic reconnection at the sun, in Magnetic Reconnection in Space and Laboratory Plasmas, Geophysical Monograph Series, Vol. 30, edited by E. W. Hones Jr. (American Geophysical Union, Washington, DC, 1984), p63.

[3] J. T. Gosling, J. Birn, and M. Hesse, Geophys. Res. Lett. 22, 869 (1995).

[4] B. U. Ö. Sonnerup, Magnetic field reconnection at the magnetopause, in Magnetic Reconnection in Space and Laboratory Plasmas, Geophysical Monograph Series, Vol. 30, edited by E. W. Hones Jr. (American Geophysical Union, Washington, DC, 1984), p92.

[5] D. H. Fairfield, J. Geophys. Res. 97, 10865 (1992).

[6] S. Machida, T. Mukai, Y. Saito, *et al.*, Geo. Res. Lett., 21, 1027 (1994)

[7] D. N. Baker, T. I. Pulkkinen, V. Angelopoulos, W. Baumjohann, and R. L. McPherron, J. Geophys. Res. 101, 12975 (1996).

[8] T. Nagai *et al.*, J. Geophys. Res. 103, 4419 (1998).

[9] F. D. Kahn and L. Brett, Mon. Not. R. Astron. Soc. 263, 37 (1993).

[10] A. W. Edwards, D. J. Campbell, *et al.*, Phys. Rev. Lett., 57, 210 (1986).

[11] R. G. Giovanelli, Nature (London) 158, 81 (1946).

[12] R. G. Giovanelli, Mon. Not. R. Astron. Soc. 107, 338 (1947).

[13] F. Hoyle, Some Recent Researches in Solar Physics, Cambridge University Press, London, 1949.

[14] J. W. Dungey, Phys. Rev. Lett. 6, 47 (1961).

[15] T. G. Cowling, Solar electrodynamics, in The Sun, ed. G. P. Kuiper, (Univ. Chicago Press, Chicago, 1953) p532.

[16] J. W. Dungey, Conditions for the occurrence of electrical discharges in astrophysical systems, Phil. Mag., Ser. 7, 44, 725 (1953).

[17] P. A. Sweet, in: Electromagnetic Phenomena in Cosmic Physics, edited by B. Lehnert (Cambridge U. Press, New York, 1958) p123.

[18] E. N. Parker, Astrophys. J. Suppl. Series 8, 77 (1963).

[19] H. E. Petschek, in AAS-NASA Symposium on the Physics of Solar Flares, edited by W. N. Hess (NASAA-SP50, Washington, 1964) p425.

[20] H. P. Furth, J. Killeen and M. N. Rosenbluth, Phys. Fluids 6, 459 (1963).

[21] F. V. Coroniti and A. Eviatar, Astrophys. J. Suppl. Ser. 33, 189 (1977).

[22] J. D. Huba, J. F. Drake and N. T. Gladd, Phys. Fluids 23, 552 (1980).

[23] L. C. Lee, Geophys. Res. Lett. 9, 1159 (1982).

[24] W. Horton and T. Tajima, Geophys. Res. Lett. 17, 123 (1990).

[25] V. M. Vasyliunas, Rev. Geophys. 13, 303 (1975).

[26] J. D. Scudder, Space Sci. Rev. 80, 235 (1997).

[27] R. Horiuchi and T. Sato, Phys. Plasmas 1, 3587 (1994).

[28] R. Horiuchi and T. Sato, Phys. Plasmas 4, 277 (1997).

[29] H. J. Cai and L. C. Lee, Phys. Plasmas 4, 509 (1997).

[30] M. Hesse, K. Schindler, J. Birn and M. Kuznetsova, Phys. Plasmas 6, 1781 (1999).

[31] M. M. Kuznetsova, M. Hesse and D. Winske, J. Geophys. Res. 105, 7601 (2000).

[32] J. W. Dungey, Noise-free neutral sheet, in Proceedings of an International Workshop in Space Plasma, vol. II, Eur. Space Agency Spec. Publ., ESA SP-285, 15 (1988).

[33] D. Biskamp, E. Schwarz, and J. F. Drake, Phys. Rev. Lett., 75, 3850 (1995).

[34] D. Biskamp, E. Schwarz, and J. F. Drake, Phys. Plasmas, 4, 1002 (1997).

[35] M. A. Shay, J. F. Drake, R. E. Dento and D. Biskamp, J. Geophys. Res., 103, 9165 (1998).

[36] M. A. Shay, J. F. Drake and B. N. Rogers, Geophys. Res. Lett. 26, 2163 (1999).

[37] E. E. Mandt, R. E. Denton and J. F. Drake, Geophys. Res. Lett., 21, 73 (1994).

[38] A. A. Galeev, in Basic Plasma Physics, edited by A. A. Galeev and R. N. Sudan (North-Holland, New York, 1984), Vol. 2, p. 305.

[39] X. Wang and A. Bhatacharjee, J. Geophys. Res. 98, 19419 (1993).

[40] K. Schindler, J. Geophys. Res. 79, 2803 (1974).

[41] J. F. Drake and Y. C. Lee, Phys. Fluids 20, 1341 (1977).

[42] G. Laval, R. Pellat, and M. Vuillemin, Plasma Physics and Controlled Fusion Research (International Atomic Energy Agency, Vienna, 1966), Vol. II, p. 259.

[43] B. Coppi, G. Laval and R. Pellat, Phys. Rev. Lett. 16, 1207 (1966).

[44] I. Katanuma and T. Kamimura, Phys. Fluids 23, 2500 (1980).

[45] W. Zwingmann, J. Wallance, K. Schindler, and J. Birn, J. Geophys. Res. 95, 20877 (1990).

[46] P. L. Pritchett, F. V. Coroniti, R. Pellat, and H. Karimabadi, J. Geophys. Res. 96, 11523 (1991).

[47] T. Sato and T. Hayashi, Phys. Fluids 22, 1189 (1979).

[48] M. Yamada, H. Ji, S. Hsu, T. Carter, R. Kulsrud and F. Trintchouk, Phys. Plasmas 7, 1781 (2000).

[49] S. C. Hsu, G. Fiksel, T. A. Carter, H. Ji, R. M. Kulsrud and M. Yamada, Phys. Rev. Lett. 84, 3859 (2000).

[50] Y. Ono, M. Yamada, T. Akao, T. Tajima and R. Matsumoto, Phys. Rev. Lett. 76, 3328 (1996).

[51] D. W. Hewett, G. E. Francis and C. E. Max, Phys. Rev. Lett. 61, 893 (1988).

[52] Z. W. Ma and A. Bhattacharjee, Geophys. Res. Lett. 23, 1673 (1996).

[53] Z. W. Ma and A. Bhattacharjee, Geophys. Res. Lett. 26, 3337 (1999).

[54] D. Krauss-Varban and N. Omidi, Geophys. Res. Lett. 22, 3271 (1995).

[55] M. Hesse and D. Winske, J. Geophys. Res. 99, 11177 (1994).

[56] H. Kitabata, T. Hayashi, T. Sato, R. Horiuchi, K. Watanabe, A. Kageyama, T. H. Watanabe, Y. Todo, and H. Takamaru, J. Phys. Soc. Japan, 65, 3208 (1996).

[57] H. Amo, T. Sato, A. Kageyama, K. Watanabe, R. Horiuchi, T. Hayashi, Y. Todo, T. H. Watanabe, and H. Takamaru, Phys. Rev., E51, 3838 (1995).

[58] C. K. Birdsall and A. B. Langdon, *Plasma Physics Via Computer Simulation* (McGraw-Hill, New York, 1985) p168.

[59] R. Courant, K. O. Friedrichs and H. Lewy, Math. Ann. 100, 32 (1928).

[60] E. G. Harris, Nuovo Cimento 23, 115 (1962).

[61] T. Terasawa, Geophys. Res. Lett., 10 475 (1983).